RSC Advances

PAPER

View Article Online
View Journal | View Issue

Check for updates

Cite this: *RSC Adv.*, 2026, **16**, 30233

$K_3Ti_2Cl_{9-x}Br_x$: structurally stable lead-free perovskites as permissive absorbers for solar cell and visible-light photocatalysis

Shahid Mehmood, *[a] Shah Rukh Khan,[a] Shaimaa A. M. Abdelmohsen,[b] Meznah M. Alanazi,*[b] Hanan Al Ghamdi[b] and Mohamed Mousa*[c]

The toxicity issues with lead-based perovskite solar cells sparked interest in lead-free alternatives, such as $K_3Ti_2Cl_{9-x}Br_x$ (x = 0, 3, 6, and 9), which are environmentally friendly. The optical, structural, and electrical properties of $K_3Ti_2Cl_{9-x}Br_x$ (x = 0, 3, 6, and 9) are investigated using density-functional theory in this study to assess their potential as absorber materials for solar cells. Phonon dispersion is used to determine the dynamical stability of these perovskites in addition to their formation energy, which further provides evidence regarding their stability. The TB-mBJ indicates its direct bandgap along the *M*–*M* direction and indirect bandgap at the *M*–*K* direction and lie within the ideal range for photoelectric conversion. The SCAPS-1D program is employed to identify the optimal solar cell designs that integrate various ETLs and HTLs. The structure with the highest power conversion efficiency out of the fifty four configurations examined is FTO/WS_2/$K_3Ti_2Cl_{9-x}Br_x$ (x = 0, 3, 6 and 9)/CuI, provides the highest performance with an efficiency of 19.11, 24.68, 25.25 and 29.00%, FF of 82.14, 81.53, 80.09 and 62.07%, V_{oc} of 1.30, 1.29, 1.25 and 1.35 V and J_{sc} of 17.84, 23.42, 25.88 and 27.00 mA cm^{-2} with the addition of recombination effect. Additionally, the effect of thickness, defect density, series and shunt resistance is also examined. Photocatalytic analysis shows that all of these compounds are capable of converting H_2O to O_2 and H_2. In the same way that the compounds under study may reduce N_2 to NH_3, they can likewise reduce CO_2 to CH_4OH and CH_4. In comparison to other materials, these compounds have an effective efficiency for reducing CO_2 and N_2 and their photocatalytic efficiency for water splitting is higher than the intended value for industrial applications. Future research should focus on developing lead-free, totally inorganic perovskite photovoltaics and photocatalysts with enhanced photovoltaic and photocatalytic performance. Such materials could have uses in photocatalysis, especially in visible light-driven processes like water splitting, CO_2 reduction, and N_2 fixation and are highly promising for use in photovoltaics and high-performance optoelectronics because they all have absorbers with strong visible-light absorption, a large PCE, and a high quantum efficiency.

Received 23rd February 2026
Accepted 28th April 2026

DOI: 10.1039/d6ra01597b

rsc.li/rsc-advances

Open Access Article. Published on 03 June 2026. Downloaded on 6/16/2026 1:54:48 AM.
This article is licensed under a Creative Commons Attribution-NonCommercial 3.0 Unported Licence.

1 Introduction

The breakthrough power conversion efficiencies (PCEs) of Pb-based halide perovskites have garnered a lot of interest.[1,2] On the other hand, concern about Pb's considerable toxicity has a negative impact on ecosystems and living things, as well as slows down the commercialization of perovskite solar cells (PSCs).[3] This is why creating perovskite materials that are free of lead is becoming a higher priority for the perovskite community. Several potential replacements to Pb that meet these criteria include halides based on Sn and Ge, double perovskites, and halides that are similar to perovskites but have lower toxicity and better optoelectrical characteristics.[3–6] Although Sn/Ge-based halides have appealing characteristics and a structure similar to Pb, their instability resulting from quick oxidation in ambient conditions is a serious constraint.[7,8]

The more stable double perovskites ($A_2BB'X_6$) have been used despite having a larger band gap than Pb-based halides.[9,10] A new class of group-VA trivalent metal cation based perovskite halides ($A_3B_2X_9$) with an electronic configuration comparable to that of Pb-based perovskites and environmentally pleasant photovoltaic device candidates and display better thermodynamic stability.[11,12] The electrical characteristics of Sb-based halides can be affected by the halide components, like Bi-based perovskite compounds that have the same problems as double perovskites. There are inherent issues with the $MA_3Sb_2I_9$ is poor carrier transport and an indirect bandgap value over 2.2 eV.[13] The mixed halide $MA_3Sb_2I_{9-x}Cl_x$[14] with theoretical

[a]*Department of Physics, University of Malakand, Chakdara, 18800, Pakistan. E-mail: shahiduom07@gmail.com*

[b]*Department of Physics, College of Science, Princess Nourah bint Abdulrahman University, P.O. Box 84428, Riyadh, 11671, Saudi Arabia. E-mail: mmalenzy@pnu.edu.sa*

[c]*Electrical Engineering Department, Future University in Egypt, Cairo, 11835, Egypt. E-mail: Mouhamed.Moussa@fu.edu.eg*

© 2026 The Author(s). Published by the Royal Society of Chemistry

Open Access Article. Published on 03 June 2026. Downloaded on 6/16/2026 1:54:48 AM. This article is licensed under a Creative Commons Attribution-NonCommercial 3.0 Unported Licence.

direct bandgap values ranging from 1.8 eV to 2.2 eV, allows for improved carrier mobility and transport when iodine is mixed with chlorine. 2D perovskite-like solar cells based on Sb still have unsatisfactory PCEs due to disordered growth, poor film shape, and uncontrolled halide components.[15,16]

Research into mixed Bi based $Cs_3Bi_2I_{9-x}Br_x$ has also focused on its potential in photovoltaics and photodetection comparatively as Sb based compounds.[17] In their study, Yu *et al.* documented a thorough investigation of the I/Br solid solution. They utilized spin coating to create thin films with end-members and intermediate mixed compositions, which were then utilized in PSCs. Although the statistics demonstrate that Bi-based phases are quite stable, the power conversion efficiencies (PCEs) are very low; the compound with the best performance, $Cs_3Bi_2I_6Br_3$, achieved 1.15%.[17] Liu *et al.*[18] investigated the photodetection capabilities of $Cs_3Bi_2Br_{9-x}I_x$ films with different values of x. The $Cs_3Bi_2I_6Br_3$ composition showed the most promising results, with a photosensitivity of 4.1×10^1 at zero bias, a responsiveness of 15 mA W^{-1}, and a detectivity of 4.6×10^5 Jones.[19] In this particular instance, remarkable environmental stability is noticed over 96% of the initial value even after 100 days. So far, all the evidence that has been reported pertains to recent research that suggests that layered perovskites made of Bi have potential for future exploration and use in various technologically significant areas. This is supported by the interest in tunable $Cs_3Bi_2(Cl_{1-x}I_x)_9$ halide perovskites.

Recently titanium in halides comparatively to Bi have taken instruct due to an interesting property of their ability to create compounds with varying valences. Solid state processes were used to produce $K_3Ti_2Cl_9$ and $K_3Ti_2Br_9$ single crystals by Schroeder *et al.*[20] The larger anions and smaller cations crating the deviance from the idealized geometry. During symmetry reductions in $K_3Ti_2Cl_9$ and $K_3Ti_2Br_9$, the $[Ti_2X_9]^{3-}$ units are rotated. For optimal outcomes, this rotation is a geometrical requirement.

Conversely the efficiency of photo-to-current conversion is restricted due to the low band gap of most perovskite semiconductors. Not only that, but they are also not suitable for use as stable photodetector materials due to their toxicity and inconsistent performance. Thus, perovskites based on titanium halide are presented as a more sustainable and environmentally friendly option for photodetection due to their extensive band gap, in order to address these important concerns. Modulating the photo response properties can probably be achieved more effectively using band gap tenability, which involves adjusting the ratio of halide ions. For the photocatalysis and solar cell application, it would be most intriguing to examine these less-studied Ti-based perovskites. A common method for modifying or altering semiconductor materials' optoelectronic and photophysical characteristics is alloying or modification. In the current study the $K_3Ti_2Cl_{9-x}Br_x$ ($x = 0$, 3, 6 and 9) have been studied to understand the Cl/Br allying and its impact on their physical properties.

2 Computational detail

This computational study used the WIEN2k software package's Full-Potential Linearized Augmented Plane Wave (FP-LAPW) approach[21] to determine the material characteristics that are

Table 1 Simulation parameters for different layers taking $K_3Ti_2Cl_{9-x}Br_x$ ($x = 0$, 3, 6, 9) perovskite as absorber layer

Parameters	FTO	WS_2 (ref. 29)	$K_3Ti_2Cl_9$[calculated]	$K_3Ti_2Cl_6Br_3$[calculated]	$K_3Ti_2Cl_3Br_6$[calculated]	$K_3Ti_2Br_9$[calculated]	CuI[29]
Thickness (nm)	300	180	900	900	900	900	150
E_g (eV)	3.5	1.80	1.86	1.64	1.56	1.51	3.10
χ_e (eV)	4.0	3.95	4.0	4.0	4.0	4.0	2.14
ε_1 (eV)	9.0	13.6	2.486	2.89	3.22	3.28	6.50
N_c (cm^{-3})	2.02×10^{19}	1×10^{18}	4.85×10^{17}	8.87×10^{15}	1.47×10^{16}	2.25×10^{15}	2.8×10^{19}
N_v (cm^{-3})	1.8×10^{19}	2.4×10^{19}	2.13×10^{18}	1.14×10^{18}	1.50×10^{18}	6.11×10^{17}	1×10^{19}
$V_{Th,e}$ (cm s^{-1})	10^7	10^7	4.34×10^7	0.96×10^8	0.98×10^8	1.48×10^7	10^7
$V_{Th,h}$ (cm s^{-1})	10^7	10^7	2.65×10^7	3.27×10^7	2.98×10^7	4.02×10^6	10^7
μ_e (m^2 V s^{-1})	2×10^1	100	80.05	183.31	258.19	495.44	100
μ_h (m^2 V s^{-1})	1×10^{-1}	100	144.34	251.11	168.17	254.60	43.9
N_D (cm^{-3})	10^{15}	0	0	0	0	0	1×10^{18}
N_A (cm^{-3})	0	10^{18}	10^{14}	10^{14}	10^{14}	10^{14}	0
N_T (cm^{-3})	10^{15}	10^{15}	10^{15}	10^{15}	10^{15}	10^{15}	10^{15}

Table 2 Simulation parameters of interface layer

Interfaces	ETL/absorber	Absorber/HTL
Type of defect	Neutral	Neutral
Cross section for electron (cm^2)	1×10^{-15}	1×10^{-15}
Cross section for hole (cm^2)	1×10^{-15}	1×10^{-15}
Energetic distribution	Single	Single
Reference of defect energy level	Above the highest E_v	Above the highest E_v
Energy level with respect to E_v (eV)	0.6	0.65
Characteristic energy (eV)	0.1	0.1
Total density (cm^{-3})	1×10^{15}	1×10^{15}

© 2026 The Author(s). Published by the Royal Society of Chemistry

Open Access Article. Published on 03 June 2026. Downloaded on 6/16/2026 1:54:48 AM.
This article is licensed under a Creative Commons Attribution-NonCommercial 3.0 Unported Licence.

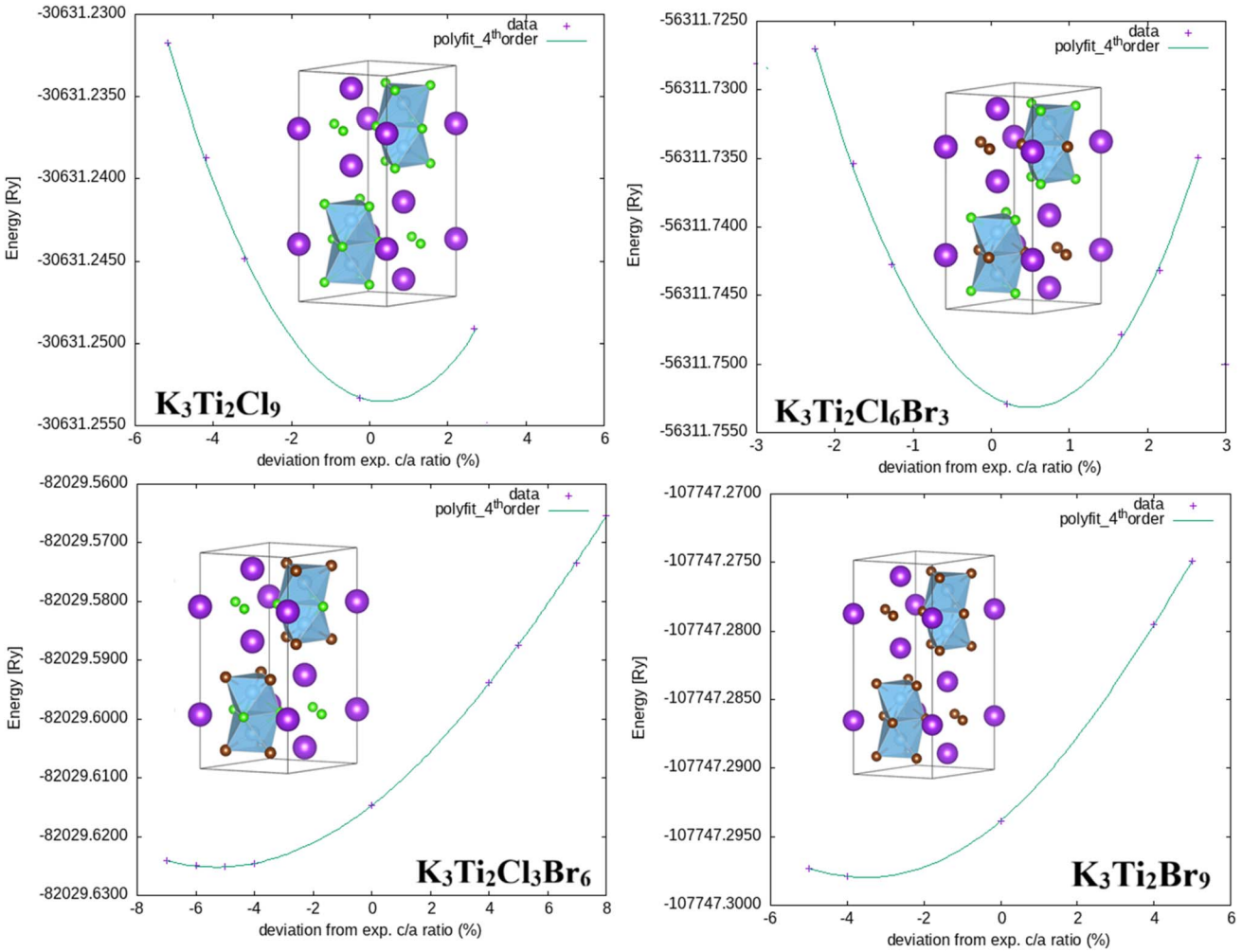

Fig. 1 Crystal structure and optimized ground state energies *versus* c/a ratio of the $K_3Ti_2Cl_{9-x}Br_x$ (x = 0, 3, 6 and 9) halide perovskites.

Table 3 Calculated lattice constants, c/a ratio, ground state energy, formation enthalpy, bond lengths, bond angels and band gap, Mulliken electronegativity CBM and VBM potentials of the $K_3Ti_2Cl_{9-x}Br_x$ (x = 0, 3, 6, 9) compounds

Parameters	$K_3Ti_2Cl_9$ (exp.)[20]	$K_3Ti_2Cl_6Br_3$	$K_3Ti_2Cl_3Br_6$	$K_3Ti_2Br_9$ (exp.)[20]
a (Å)	7.128 (7.073, 7.052)	7.17	7.28	7.387 (7.429, 7.406)
c (Å)	17.430 (17.544, 17.491)	17.68	17.84	18.295 (18.382, 18.330)
c/a	2.48 (2.50)	2.46	2.45	2.38 (2.47)
E_0 (Ry)	−30631.254	−56311.7500	−82029.6252	−107747.297
T	1.01	1.00	0.998	0.992
μ	0.334	0.325	0.317	0.301
H_f (Ry)	−0.224	−0.252	−0.272	−0.287
E_g (eV)	1.861, 1.861	1.643, 1.648	1.567, 1.577	1.512, 1.519
For direct nature				
m_e^*	$0.229m_e$	$0.060m_e$	$0.131m_e$	$0.037m_e$
m_h^*	$0.127m_e$	$0.084m_e$	$0.153m_e$	$0.072m_e$
For indirect nature				
m_e^*	$0.209m_e$	$0.100m_e$	$0.071m_e$	$0.100m_e$
m_h^*	$0.187m_e$	$0.073m_e$	$0.109m_e$	$0.193m_e$
E_b (meV)	66.28	10.63	8.78	3.18
a^* (Å)	33.15	273.22	254.95	784.08
χ_{com}	5.313	5.263	5.214	5.166
E_{CB}	−0.056	−0.06	−0.015	−0.038
E_{VB}	1.783	1.633	1.544	1.471

© 2026 The Author(s). Published by the Royal Society of Chemistry

Open Access Article. Published on 03 June 2026. Downloaded on 6/16/2026 1:54:48 AM.
This article is licensed under a Creative Commons Attribution-NonCommercial 3.0 Unported Licence.

desired. In order to accurately calculate the density of states (DOS) and explain optical and electrical properties, the Trans-Blaha modified Becke-Johnson (TB-mBJ) method[22] was used. The generalized gradient approximation (GGA)[23] an exchange–correlation potential were used for structural property calculations. A number of FP-LAPW basis functions were investigated, with RMT spheres set to 8 as an example. The muffin-tin spheres had their spherical harmonics magnified to $L_{max} = 11$, and their Fourier-expanded charge densities were capped at $G_{max} = 12$ (a.u.). For self-consistent field calculations,

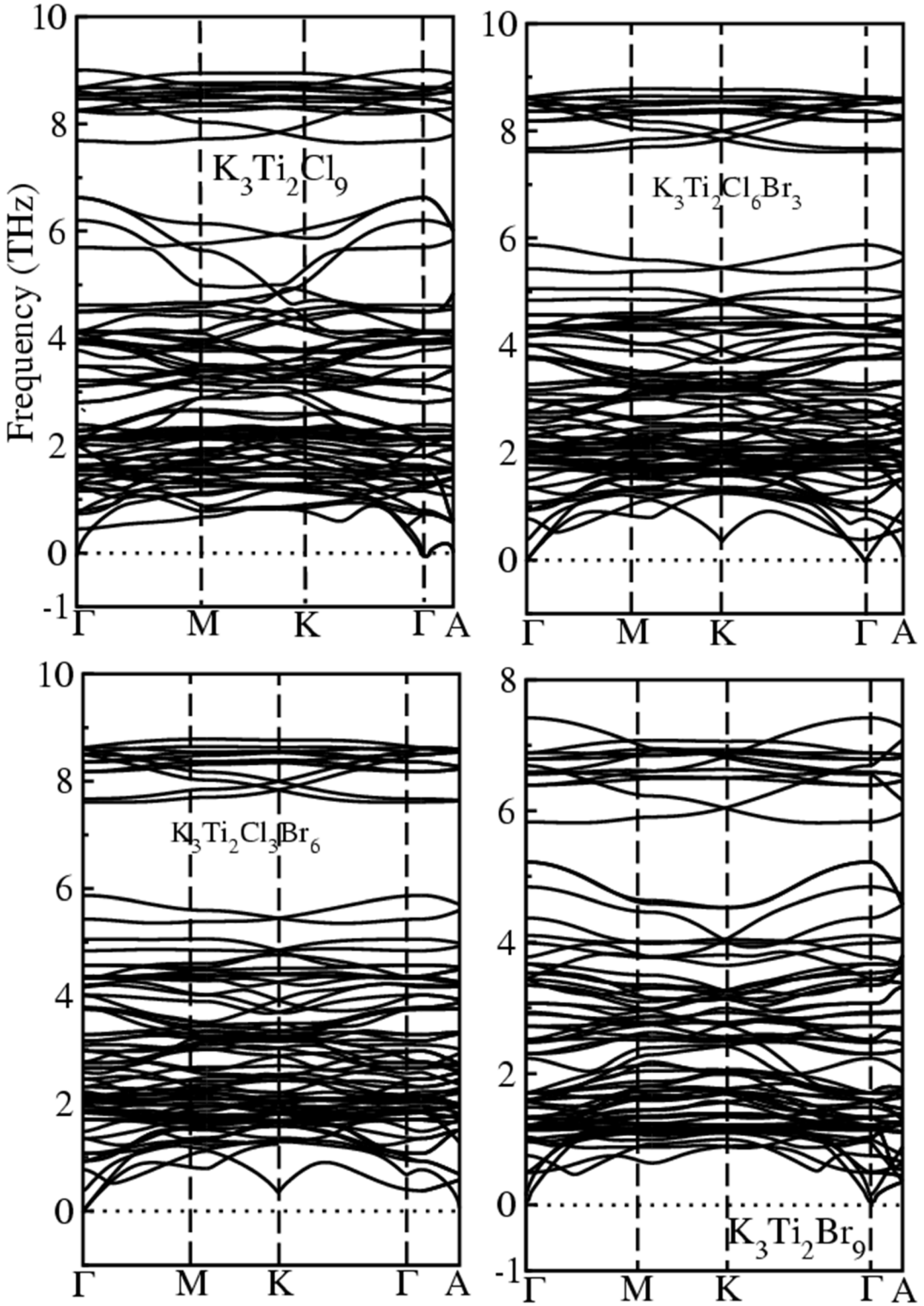

Fig. 2 Phonon dispersion curves of the $K_3Ti_2Cl_{9-x}Br_x$ ($x = 0$, 3, 6 and 9) halide perovskites.

© 2026 The Author(s). Published by the Royal Society of Chemistry

Open Access Article. Published on 03 June 2026. Downloaded on 6/16/2026 1:54:48 AM. This article is licensed under a Creative Commons Attribution-NonCommercial 3.0 Unported Licence.

convergence was defined as a total energy variation less than or equal to 0.0001 Ry. The energy–volume curve was fitted using the Birch–Murnaghan equation of state,[24] which allowed the estimation of equilibrium lattice parameters. To further understand the possible optoelectronic applications of the chosen crystalline materials, their optical behavior was investigated using the dielectric function.[25] The photocatalytic performance of these compounds are calculated using Mullikan electronegativity method[26] and the solar to energy conversion efficiency is calculated by the formula $\eta_{STC} = \frac{(J_{SC} \times \Delta G \times \eta_F) \times 100}{P_{in}}$.[27] The variables J_{sc}, ΔG, η_F, and P_{in} represent the current density, Gibbs free energy, faradaic efficiency and input power and the η_F is assumed to be one, the upper limit in this equation. Analytical determination of ΔG is made using the conversion reaction for water splitting, CO_2 reduction, and N_2 fixation.

The study of PV performance, including J_{sc}, V_{oc}, FF, and PCE of the designed solar cells are investigated and modeled by employing the SCAPS simulation software.[28] A light power of 1000 W m^{-2} spectrum is employed for the simulations, which were conducted at 300 K and the simulation parameters are given in Table 1 and 2 correspondingly.[29,30]

3 Results and discussion

3.1 Structural properties

In the current study, the compounds $K_3Ti_2Cl_{9-x}Br_x$ (x = 0, 3, 6 and 9) have a hexagonal crystal with space group $P6_3/m$ (no. 176) and belong to $K_3W_2Cl_9$ type crystal is shown in Fig. 1. In these perovskite-related structures the monovalent cations K as large as the halide anions Cl and Br and have a K : Cl or Br is of 1 : 3. Ti cations fill the octahedral spaces created by anions in hexagonal sequences but are absent in cubic sequences. Separate face-sharing octahedra [Ti_2Cl_9 or Br_9] are the most noticeable structural element in these compounds and therefore these compounds are of great interest due to Ti–Ti interactions owing to the proximity of the Ti atom.

The total energy was determined by plotting it against the c/a ratio in order to study the structural behavior and analyze its ground-state characteristics. To find their optimum ground state lattice constants, all these compounds were subjected to single-point computations. The Birch–Murnaghan equation of state is used to determine the optimized lattice constants (a and c).[31] The actual lowest ground state of the compound is represented by the minimum energy E_0, and their structural stability is enhanced by the negative energy values. The optimized structural parameters are shown in Table 3. The changes in cell

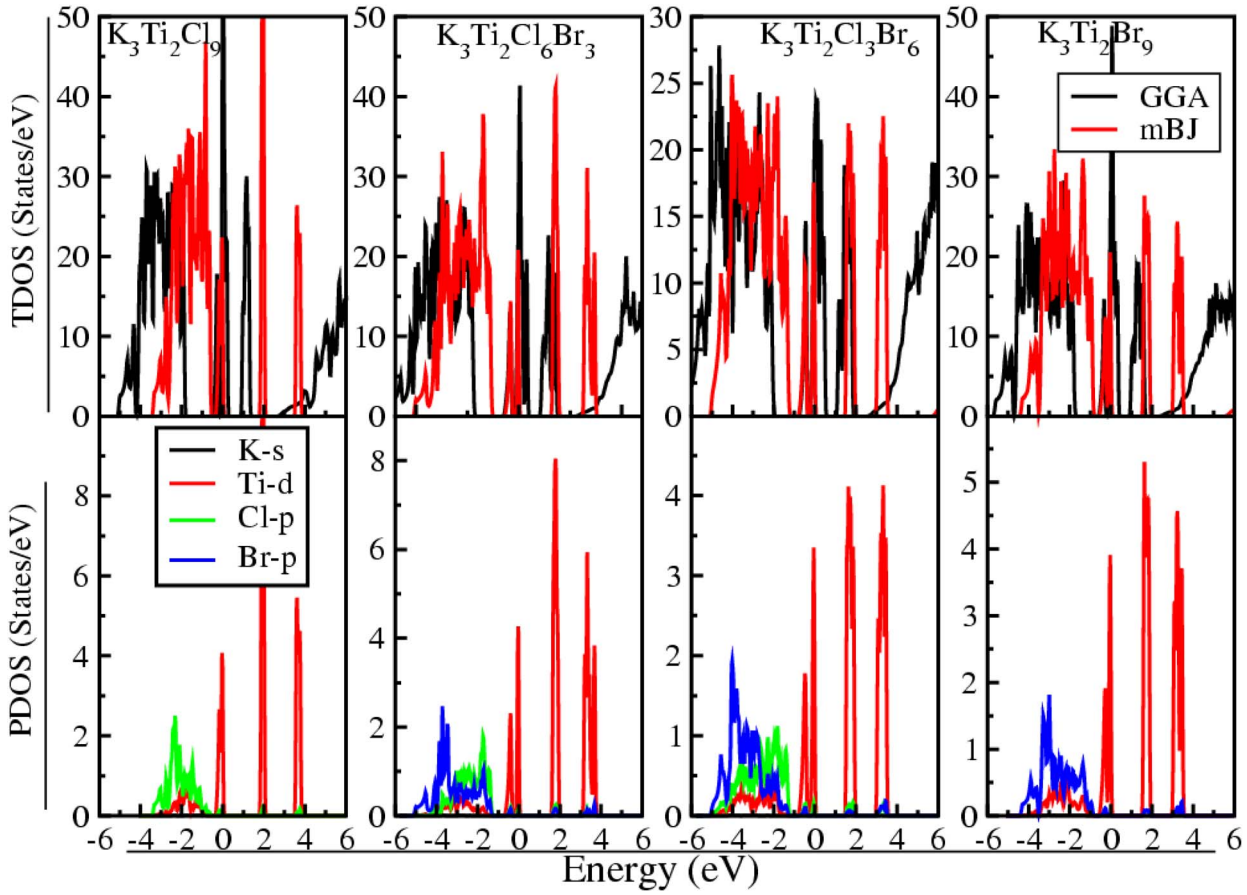

Fig. 3 Total DOSs and partial DOSs of the $K_3Ti_2Cl_{9-x}Br_x$ (x = 0, 3, 6 and 9) halide perovskites.

Open Access Article. Published on 03 June 2026. Downloaded on 6/16/2026 1:54:48 AM.
This article is licensed under a Creative Commons Attribution-NonCommercial 3.0 Unported Licence.

characteristics from Cl to Br are in line with the cations' increasing ionic radii. As a contrast to Br, Cl has a smaller ionic radius. Both the cell size trend and the ionic sizes of these cations are in excellent agreement. Fig. 1 shows the optimization curve for all these compounds, and the lowering of energy value from Cl-based to Br-based compounds suggests increased structural stability. On the other hand, the tolerance and octahedral factors for these compounds are also calculated and found to be in the stable range for these compounds.[32] In addition, the formation enthalpy (H_f) is computed in order to evaluate the formation feasibility. Their structural stability is further confirmed by the negative formation energies, which indicate that the production of these compounds is energetically satisfactory.[33] The studied compounds show negative formation energies, which indicates these compounds are energetically favorable, according to the computed values in Table 3.

On the other hand for specialized device performance, it is essential to evaluate a material's dynamic stability. This has been accomplished by working with the WIEN2k using the Phonopy code.[34] Theoretically, when the basic unit cell of a material contains n atoms, the resulting phonon spectrum will show $3n$ different branches.[35] Three of the peaks on this spectrum are directly related to acoustic phonon modes, and the other $3n$-3 peaks are directly related to optical phonon modes. A material's intrinsic physical qualities and behavior

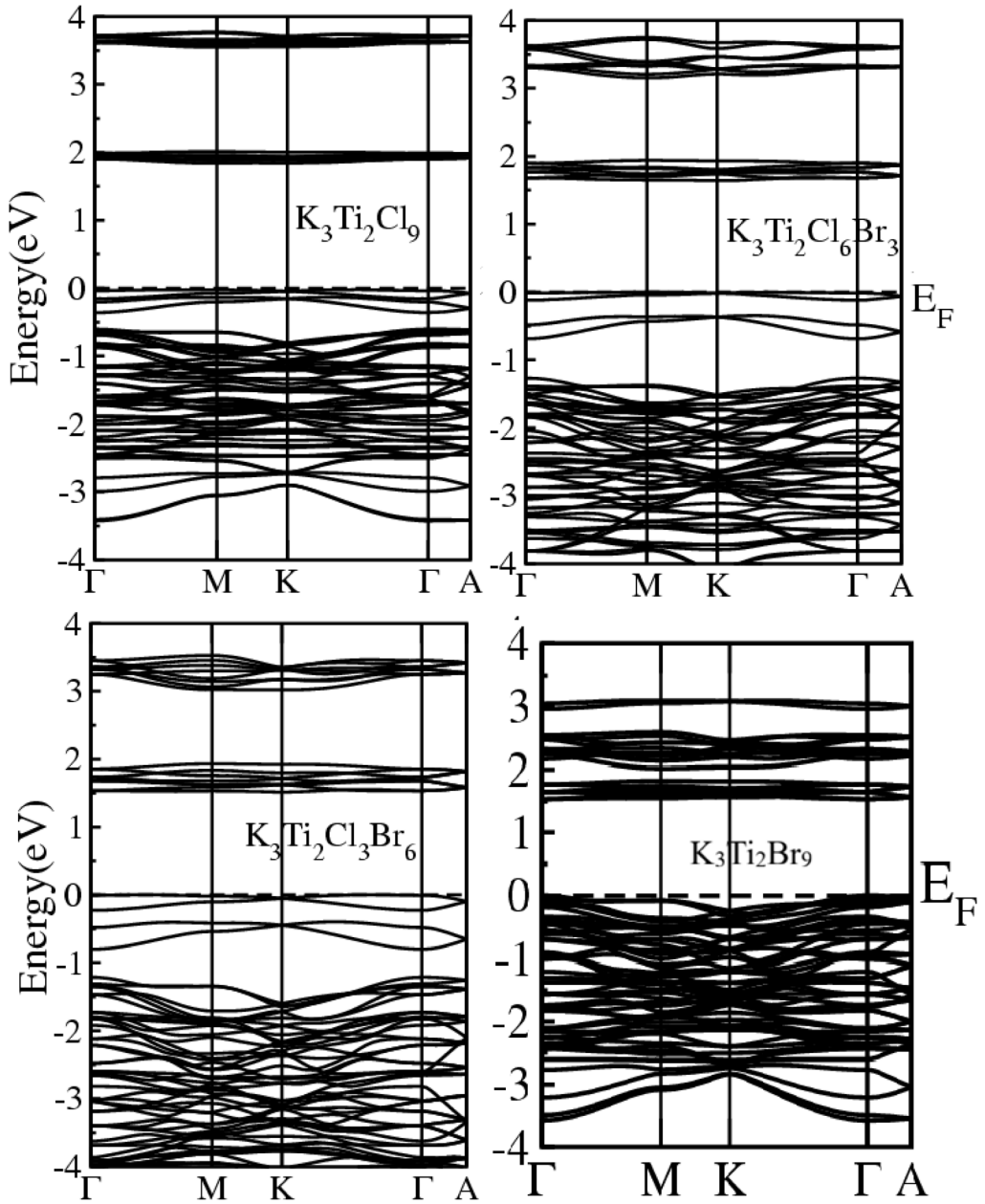

Fig. 4 Electronic band structure of the $K_3Ti_2Cl_{9-x}Br_x$ (x = 0, 3, 6 and 9) halide perovskites.

© 2026 The Author(s). Published by the Royal Society of Chemistry

Open Access Article. Published on 03 June 2026. Downloaded on 6/16/2026 1:54:48 AM.
This article is licensed under a Creative Commons Attribution-NonCommercial 3.0 Unported Licence.

can be understood by using this concept, which sheds light on the complex connection between the atomic make-up of a material's unit cell and the unique vibrational modes exhibited by its individual atoms. The materials under study have a basic unit cell structure with 14 atoms, which causes them to exhibit 42 different vibrational modes, as illustrated in Fig. 2. The three curves that show the lowest frequencies at the Γ point depict the acoustic branch lattice waves, which are in the frequency range of sound waves. The remaining 39 curves among the 42 represent the lattice waves of the optical branch. The figure illustrates that phonon dispersion curves for all compounds are above zero and does not found imaginary frequencies, which further confirms the stability of the under study compounds. Based on this finding, it may be concluded that these materials have dynamically stable materials. In addition, the phonon dispersion curves do not include imaginary frequencies indicating that the materials under study are not prone to phase transitions or structural distortions at the analyzed pressure and temperature conditions. Based on these results, it appears that these materials are dynamically stable for use in high-performance devices.

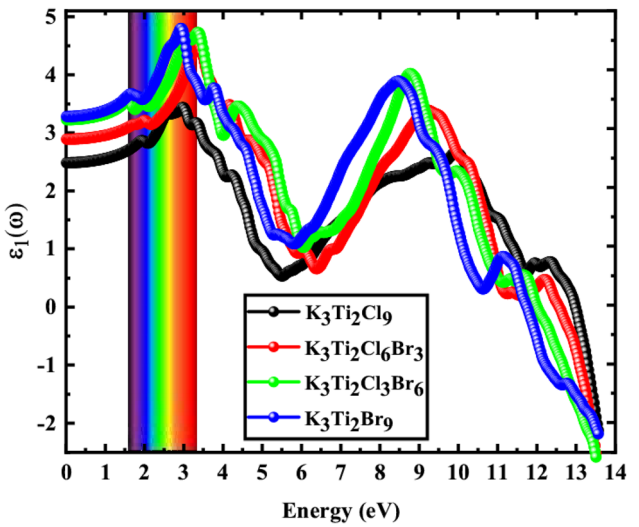

Fig. 5 Real part of dielectric function of the $K_3Ti_2Cl_{9-x}Br_x$ (x = 0, 3, 6 and 9) halide perovskites.

3.2 Electronic properties

To fully grasp the potential of $K_3Ti_2Cl_{9-x}Br_x$ (x = 0, 3, 6 and 9) compounds in optoelectronic and solar cell applications, a systematic understanding of their electronic band structure is essential. The electronic behavior of the under study compounds are explained with the help of total density of states (DOS) estimated *via* GGA and mBJ revealed in Fig. 3, which reveals that the densities do not overlap at the Fermi level and do not encompass the VB to the CB indicate the semiconductor

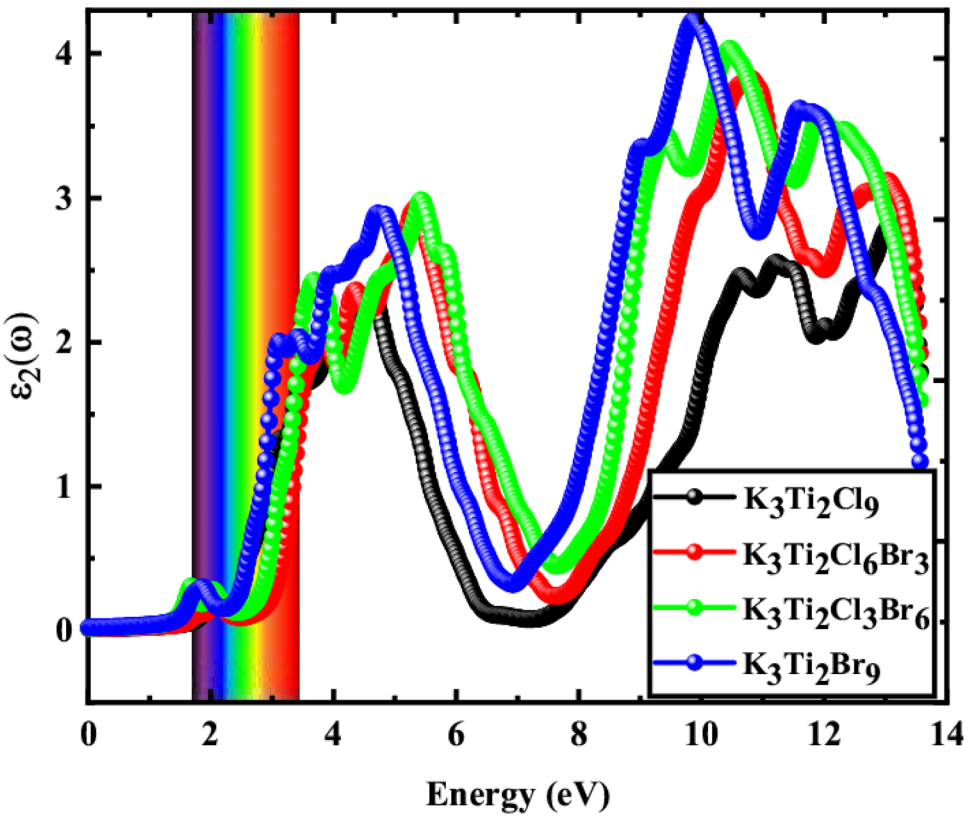

Fig. 6 Imaginary part of dielectric function of the $K_3Ti_2Cl_{9-x}Br_x$ (x = 0, 3, 6 and 9) halide perovskites.

Open Access Article. Published on 03 June 2026. Downloaded on 6/16/2026 1:54:48 AM.
This article is licensed under a Creative Commons Attribution-NonCommercial 3.0 Unported Licence.

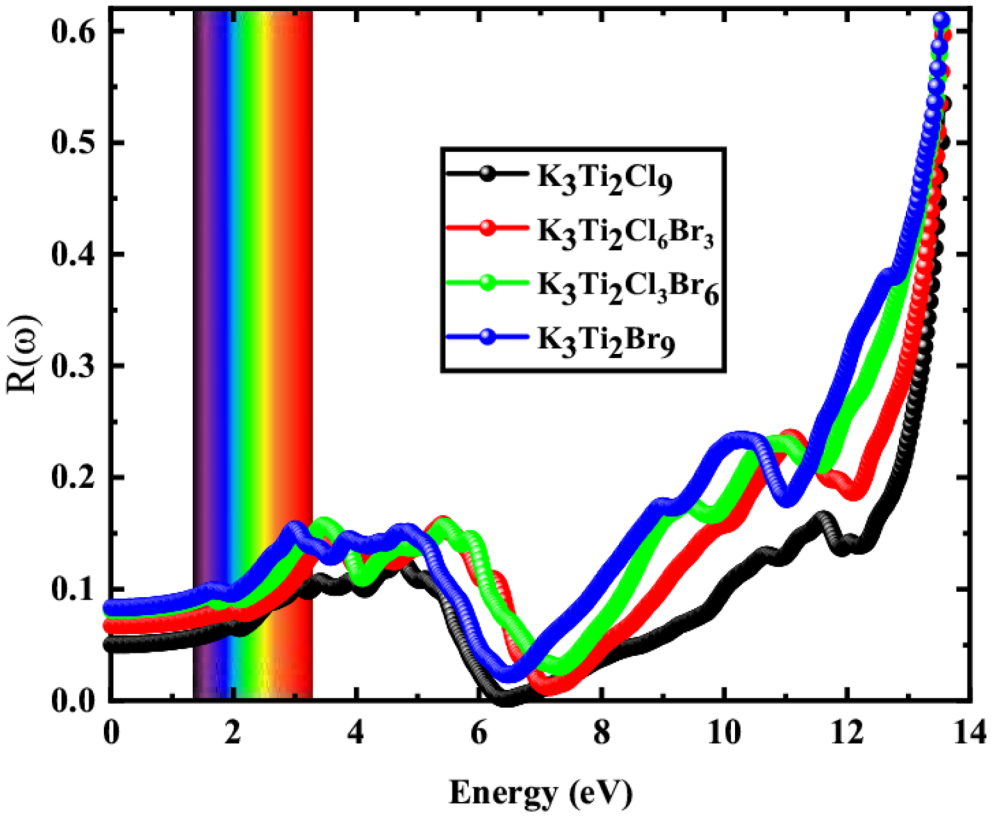

Fig. 7 Absorption of the $K_3Ti_2Cl_{9-x}Br_x$ (x = 0, 3, 6 and 9) halide perovskites.

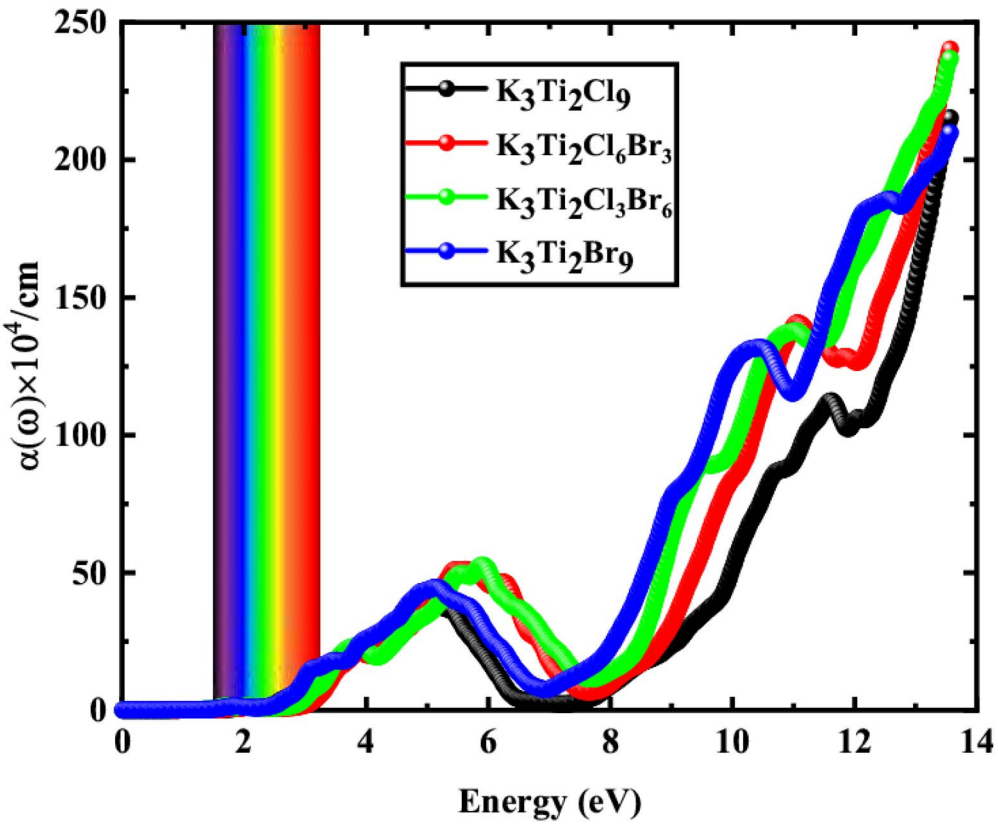

Fig. 8 Reflectivity of the $K_3Ti_2Cl_{9-x}Br_x$ (x = 0, 3, 6 and 9) halide perovskites.

© 2026 The Author(s). Published by the Royal Society of Chemistry

Open Access Article. Published on 03 June 2026. Downloaded on 6/16/2026 1:54:48 AM. This article is licensed under a Creative Commons Attribution-NonCommercial 3.0 Unported Licence.

nature of these compounds through mBJ, while the GGA indicates their metallic nature. In order to further validate the electronic nature of the compounds, their TDOS is also calculated by applying Hubbard U with GGA, SOC and HSE06 and given in Fig. S1. The obtained results also indicate the semiconductor nature of these compounds with minor changes in their band gaps accordingly.

Fig. 4 shows the electronic band structure for $K_3Ti_2Cl_{9-x}Br_x$ ($x = 0$, 3, 6 and 9) respectively. The horizontal dashed line shows the Fermi level at 0 eV. The electronic band structure is computed over the representative directions of high symmetry k-points (Γ–M–K–Γ–A) in the first Brillouin zone for $K_3Ti_2Cl_{9-x}Br_x$ ($x = 0$, 3, 6 and 9) perovskite as depicted in Fig. 4. The band gap (E_g) of $K_3Ti_2Cl_{9-x}Br_x$ ($x = 0$, 3, 6 and 9) compound, with mBJ functional is determined over the high-symmetry k-lines in the first Brillouin zone, indicating its direct bandgap of 1.861, 1.648 and 1.577 eV along the M–M direction and 1.519 eV along the Γ–Γ direction and indirect E_g of 1.861, 1.643, and 1.567 eV at the M–K direction and 1.512 eV at the Γ–M direction. The difference among the direct and indirect E_g is 0.00, 0.005, 0.01 and 0.007 eV accordingly in these compounds are of unique character and both the direct and indirect E_g of the $K_3Ti_2Cl_{9-x}Br_x$ ($x = 0$, 3, 6 and 9) semiconductor is associated with the absorption span in the visible light, which may yield a PV quantum effect in inter-bands with better efficiency.[36] A similar effect of electronic transition *via* atomic doping is also reported for double perovskites.[37,38]

Moreover, the projected density of states (PDOS) on s, p, d states of K, Cl, Br and Ti atoms respectively for $K_3Ti_2Cl_{9-x}Br_x$ ($x = 0$, 3, 6 and 9) perovskites are computed. As plotted in Fig. 3, the PDOS results reveal four regions of energy states of the studied compounds. The plot displays two portions of valence bands (VB) that range between −5.5 eV and EF. The major portion of PDOS of the various s, p, and d states of K, Cl, Br and Ti atomic elements participated in the VB. Remarkably, the two sections situated upward the EF in the positive range of energy states are delineated by the conduction bands (CB). The lowest valence states that are mainly assisted by a sharp spectral peak of Cl and Br-p states are around −5.5 to 1 eV and are overlapped with a small contribution of d orbitals of the Ti atom. A significant hybridization of Ti-d state occur with the Cl and Br-p states that participate to form the valence states edge. The next section is composed of a weak assistance of states of the Ti element centered at about −1 to 0 eV. On the other hand the CB is composed of the Ti-d state in the two sections from E_g to 2 eV and from 3 to 4 eV respectively.

3.3 The effective mass, exciton binding energy and radius

Diffusion length, electrical conductivity, carrier mobility, and effective mass of charge carriers are the fundamental variables

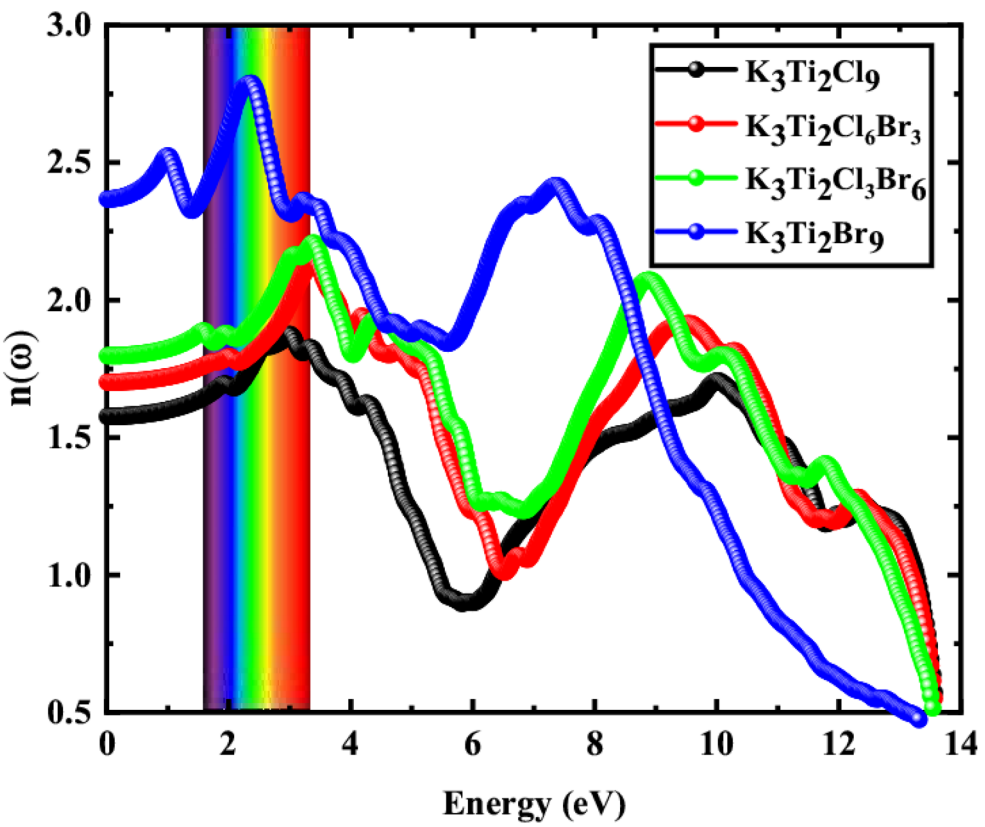

Fig. 9 Refractive index of the $K_3Ti_2Cl_{9-x}Br_x$ ($x = 0$, 3, 6 and 9) halide perovskites.

Open Access Article. Published on 03 June 2026. Downloaded on 6/16/2026 1:54:48 AM.
This article is licensed under a Creative Commons Attribution-NonCommercial 3.0 Unported Licence.

that have a direct impact on the transport properties of semiconductors. The curvature of the electronic band diagram around the VBM and CBM, respectively, is used to compute the effective mass of holes m_h^* and electrons m_e^* for $K_3Ti_2Cl_{9-x}Br_x$ (x = 0, 3, 6 and 9). Band topologies with relatively distributed valence bands around the EF are shown in Fig. 4. This suggests

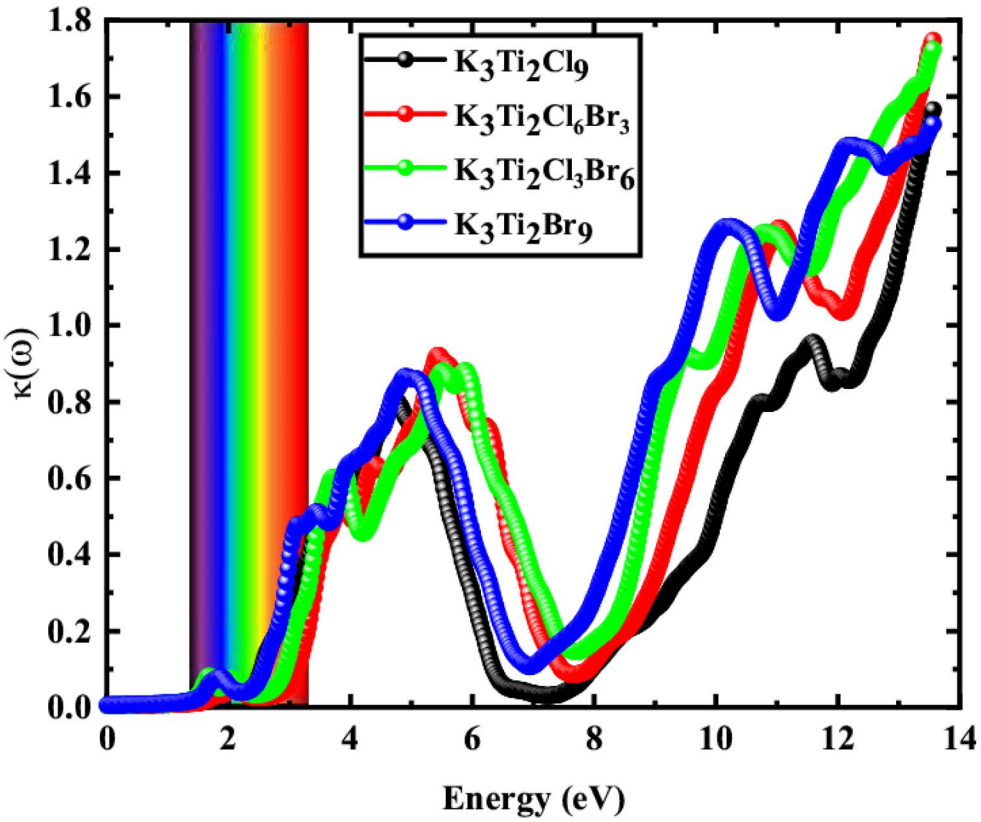

Fig. 10 Excitation coefficient of the $K_3Ti_2Cl_{9-x}Br_x$ (x = 0, 3, 6 and 9) halide perovskites.

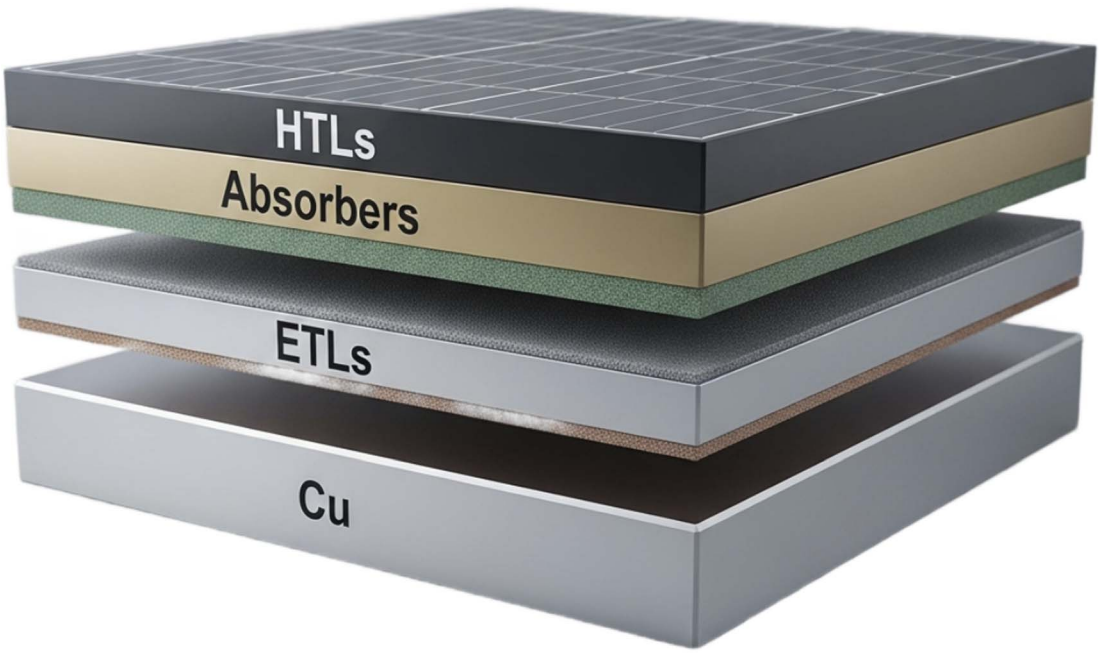

Fig. 11 Schematic solar cell model of the $K_3Ti_2Cl_{9-x}Br_x$ (x = 0, 3, 6 and 9) halide perovskites.

© 2026 The Author(s). Published by the Royal Society of Chemistry

Open Access Article. Published on 03 June 2026. Downloaded on 6/16/2026 1:54:48 AM. This article is licensed under a Creative Commons Attribution-NonCommercial 3.0 Unported Licence.

that the m_e^* is lower than the m_h^*, which is beneficial for effective charge transfer, as specified in Table 3. The values of m_e^* for the $K_3Ti_2Cl_{9-x}Br_x$ ($x = 0$, 3, 6 and 9) compounds are 0.229 m_e, 0.100 m_e, 0.071 m_e and 0.037 m_e, while the m_h^* is 0.127 m_e, 0.073 m_e, 0.109 m_e and 0.072 m_e, as shown in Table 3. This indicates the compounds with the lowest effective mass and the highest carrier mobility and are consistent with the effective masses for electrons and holes reported for isotropic compounds.[39,40]

It is expected that $K_3Ti_2Cl_{9-x}Br_x$ ($x = 0$, 3, 6 and 9) compounds, which have lighter effective masses and lower E_g, will have higher light absorption and increased carrier mobility, as a result of the equilibrium between the two variables controlling their transport properties. Consequently, $K_3Ti_2Cl_{9-x}Br_x$ ($x = 0$, 3, 6 and 9) might be the best which would make it a viable option for SCs and optoelectronic applications. Additionally, the exciton radius (a^*) and exciton binding energy (E_b) are determined for these compounds to study their excitonic properties. An estimated value of E_b for these compounds are 66.28, 10.63, 8.78 and 3.18 meV component respectively show in Table 3. Table 3 also displays a^* these compounds, which are 33.15, 273.22, 254.95 and 784.08 Å respectively. From Table 3, it is clear that the a^* is increasing with decreases E_b. The photogenerated electron and hole charge carriers have a larger a^* and a lower exciton E_b, which are advantageous for SC applications since they interact less and disintegrate faster. The compounds under investigation show outstanding potential as SC and photocatalytic materials because of their remarkable E_g, electron mobility, reduced effective mass, decreased exciton energy, and increased exciton radius as a Pb-free alternative.

3.4 Optical properties

Since the semiconducting compounds with direct band gaps, are optically active materials, it is crucial to provide a detailed explanation of their optical characteristics. The dielectric function $\varepsilon(\omega)$, which represents the polarization of light response to the material, serves to determine the corresponding optical characteristics. $\varepsilon(\omega)$ composed of two components, the real and imaginary. The imaginary component $\varepsilon_2(\omega)$ of the dielectric function is simulated using the joint DOS along the first-Brillouin zone, whereas the real part $\varepsilon_1(\omega)$ is connected to

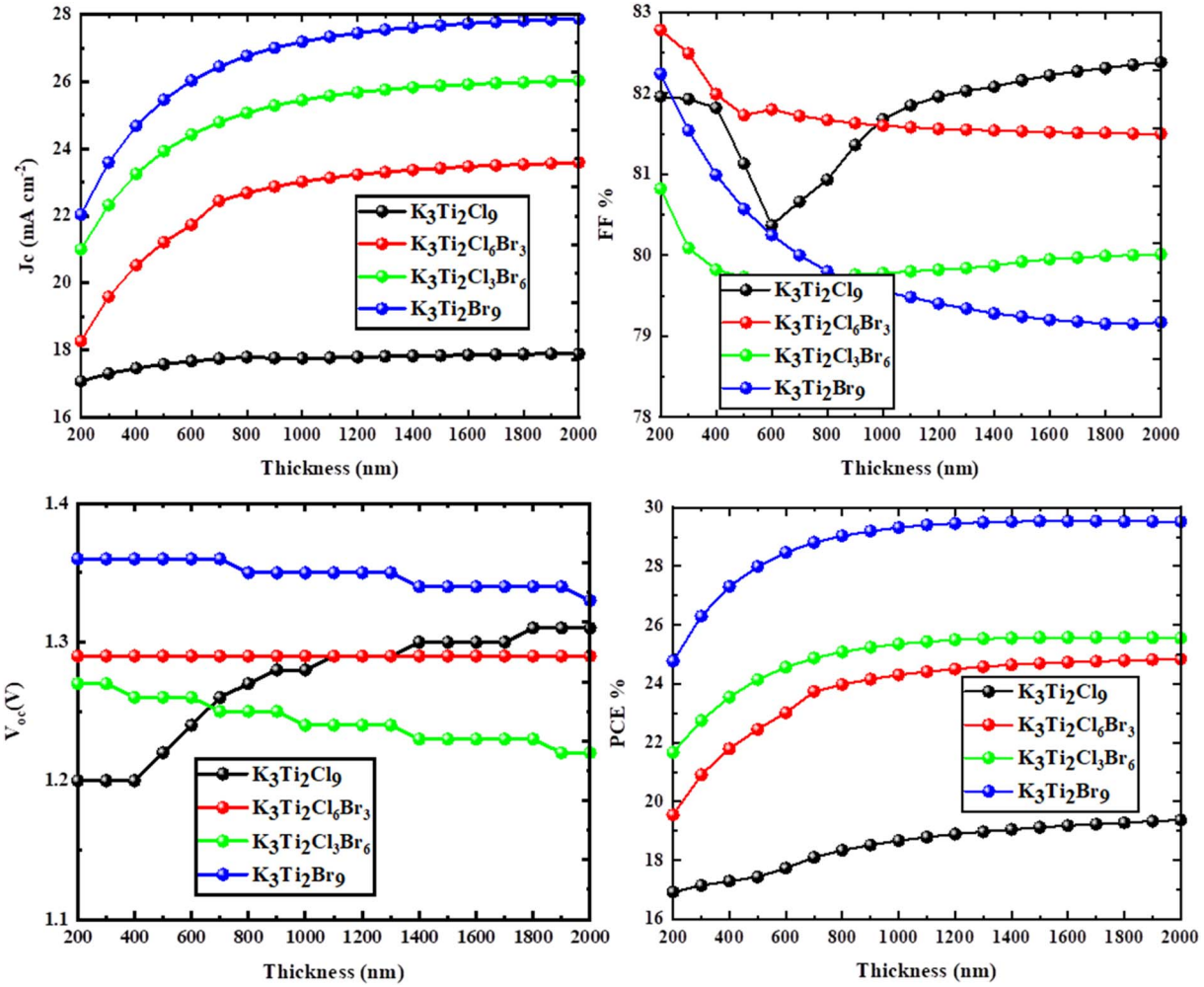

Fig. 12 Effect of absorber thickness on the PV parameters of the $K_3Ti_2Cl_{9-x}Br_x$ ($x = 0$, 3, 6 and 9) halide perovskites.

Open Access Article. Published on 03 June 2026. Downloaded on 6/16/2026 1:54:48 AM. This article is licensed under a Creative Commons Attribution-NonCommercial 3.0 Unported Licence.

Table 4 Simulation parameters of CuI as HTL with different ETL for $K_3Ti_2Cl_{9-x}Br_x$ (x = 0, 3, 6, 9) perovskite as absorber layer

HTL	ETL	Absorber	V_{oc} (V)	J_C (mA cm^{-2})	FF (%)	PCE (%)
CuI	TiO_2	$K_3Ti_2Cl_9$	1.147	16.00	76.48	14.04
		$K_3Ti_2Cl_6Br_3$	1.10	22.40	76.73	18.99
		$K_3Ti_2Cl_3Br_6$	1.04	24.88	74.02	19.30
		$K_3Ti_2Br_9$	1.00	26.61	72.53	19.37
	Li-TiO_2	$K_3Ti_2Cl_9$	1.17	16.20	74.89	14.30
		$K_3Ti_2Cl_6Br_3$	1.10	22.76	77.57	19.56
		$K_3Ti_2Cl_3Br_6$	1.04	25.23	75.63	19.86
		$K_3Ti_2Br_9$	0.99	26.97	74.47	19.95
	ZnO	$K_3Ti_2Cl_9$	1.16	16.30	75.94	14.39
		$K_3Ti_2Cl_6Br_3$	1.11	22.76	76.24	19.28
		$K_3Ti_2Cl_3Br_6$	1.05	25.23	73.71	19.54
		$K_3Ti_2Br_9$	1.00	26.96	72.32	19.62
	Al-ZnO	$K_3Ti_2Cl_9$	1.16	16.32	76.38	14.51
		$K_3Ti_2Cl_6Br_3$	1.12	22.61	77.18	19.61
		$K_3Ti_2Cl_3Br_6$	1.06	25.22	74.39	20.00
		$K_3Ti_2Br_9$	1.02	26.95	73.00	20.11
	WS_2	$K_3Ti_2Cl_9$	1.28	17.77	81.36	18.52
		$K_3Ti_2Cl_6Br_3$	1.29	22.87	81.63	24.16
		$K_3Ti_2Cl_3Br_6$	1.25	25.29	79.76	25.25
		$K_3Ti_2Br_9$	1.35	27.00	79.58	29.34
	PCBM	$K_3Ti_2Cl_9$	1.16	16.31	78.25	14.86
		$K_3Ti_2Cl_6Br_3$	1.11	22.71	77.33	19.52
		$K_3Ti_2Cl_3Br_6$	1.04	25.17	75.21	19.82
		$K_3Ti_2Br_9$	1.00	26.89	73.92	19.91

the imaginary component *via* the Kramers–Kronig relation.[41] Both $\varepsilon_1(\omega)$ and $\varepsilon_2(\omega)$ components are useful for computing all the important optical constants, including reflectivity coefficient $R(\omega)$, the refractive index $n(\omega)$, and the optical absorption coefficient $\alpha(\omega)$, and so forth.

The peak values of $\varepsilon_1(\omega)$ show the materials' noticeable optical characteristics in the visible and ultraviolet region. This is in agreement with Penn's hypothesis, which postulates that static polarization and the E_g are inversely related.[42] The static ε denoted as SDF is represented by the expression ($\varepsilon_1(0)$) at zero frequency. SDF for $K_3Ti_2Cl_9$ is 2.48, 2.89 for $K_3Ti_2Cl_6Br_3$, 3.22 for $K_3Ti_2Cl_3Br_6$ and for $K_3Ti_2Br_9$ is 3.28 respectively as visible in Fig. 5. As can be seen in Fig. 5, a peaking of the spectra for $K_3Ti_2Cl_{9-x}Br_x$ (where x = 0, 3, 6, and 9) occurred at 2.97, 3.36, 3.33, and 2.95 eV, respectively, after the zero frequency. After reaching their peak, the spectra progressively decline until they drop below zero. When this happens, the compounds lose their dielectric nature and start behaving more like metals.

The imaginary part $\varepsilon_2(\omega)$ of dielectric function representing light absorption and energy dissipation is shown in Fig. 6. It can be seen that at the beginning $\varepsilon_2(\omega)$ is zero so light absorption is zero after that the light absorption starts at the E_g value. After the E_g value the $\varepsilon_2(\omega)$ reaches its greatest value at particular photon intensities. These peaks show possible light-energy absorptions that result in interband transitions.

The optical absorption coefficient describes the amount of light absorbed when the electromagnetic radiation with sufficient photon energy is incident upon the material. Electrons will absorb photons in the valence band of a semiconducting material with energies exceeding the band gap, thereby transiting to the conduction band. The efficiency of SC possesses an essential reliance on the details of the VB and CB edges. Fig. 7 exhibits the absorption coefficient spectrum for these compounds. As shown in Fig. 7, the absorption edge starts at an energy value approximately at the band gap. It is illustrated in Fig. 7, that the maximal peak features appear in the energy range between 9.5 and 13.95 eV for these compounds. The absorption coefficient reveals that the compounds have a much larger optical absorption coefficient exceeding 10^4 cm^{-1} in the visible spectrum, which could serve as an appealing characteristic for SC applications.[43] This can make this semiconductor perfect, as a light-absorbing material beneficial for the thin-film PV devices.

The linear optical response from VBs to the lowest CBs is delineated *via* the reflectivity. As is apparent, the reflectivity

Table 5 Simulation parameters of CuI as HTL with different ETL for $K_3Ti_2Cl_{9-x}Br_x$ (x = 0, 3, 6, 9) perovskite as absorber layer

HTL	ETL	Absorber	V_{oc} (V)	J_C (mA cm^{-2})	FF (%)	PCE (%)
CuI	SnO_2	$K_3Ti_2Cl_9$	1.16	16.33	76.42	14.50
		$K_3Ti_2Cl_6Br_3$	1.11	22.72	77.27	19.59
		$K_3Ti_2Cl_3Br_6$	1.03	25.19	75.80	19.69
		$K_3Ti_2Br_9$	1.09	21.76	78.37	18.71
	IGZO	$K_3Ti_2Cl_9$	1.15	16.31	75.19	14.21
		$K_3Ti_2Cl_6Br_3$	1.06	22.76	75.22	18.22
		$K_3Ti_2Cl_3Br_6$	0.99	25.23	72.85	18.28
		$K_3Ti_2Br_9$	0.94	26.96	71.29	18.25
	PCBM-PCPB	$K_3Ti_2Cl_9$	1.17	16.31	76.66	14.70
		$K_3Ti_2Cl_6Br_3$	1.12	22.71	74.70	19.07
		$K_3Ti_2Cl_3Br_6$	1.05	25.17	72.13	19.24
		K_3Ti_2 Br $_9$	1.01	26.89	70.55	19.22
	TiO_2-SnO_2	$K_3Ti_2Cl_9$	1.15	16.26	76.81	14.47
		$K_3Ti_2Cl_6Br_3$	1.11	22.64	77.39	19.58
		$K_3Ti_2Cl_3Br_6$	1.06	25.11	74.73	19.94
		K_3Ti_2Br $_9$	1.06	25.11	74.71	20.06

© 2026 The Author(s). Published by the Royal Society of Chemistry

Open Access Article. Published on 03 June 2026. Downloaded on 6/16/2026 1:54:48 AM. This article is licensed under a Creative Commons Attribution-NonCommercial 3.0 Unported Licence.

spectrum of the stannite structure is depicted in Fig. 8. The occurrence of a prominent peak is around 13.95 eV for these compounds. The static spectral components of the optical reflectivity $R(0)$ are 5.0, 6.7, 8.1 and 8.3% for $K_3Ti_2Cl_{9-x}Br_x$ (x = 0, 3, 6 and 9) compound.

Refractive index $n(\omega)$ measures the transparency and has an essential impact on devices such as SCs.[44] The optical characteristic of a material whose $n(\omega)$ is dependent on the direction of light propagation and polarization is referred to as birefringence.[45] The orientation of the crystalline lattice with respect to the incident light determines whether the optically anisotropic materials interact with light through their crystallographically different axes. A notable feature n(0) the static $n(\omega)$ for these compounds is 1.57, 1.70, 1.79 and 2.36 shown in Fig. 9. The refractive index spectrum *versus* the photon energy increases and then decreases with a few oscillations (at high photon energies).

To quantify a material's absorption and scattering properties extinction coefficient $k(\omega)$ for these compounds is also calculated and shown in Fig. 10. A stronger absorption of light is indicated by higher values of $k(\omega)$. After E_g value the $k(\omega)$ grows and achieves a maximum value at 4.79 to 5.89, 10.21 to 11.63 and at 13.56 eV correspondingly for $K_3Ti_2Cl_{9-x}Br_x$ (x = 0, 3, 6 and 9) compounds, indicating that these compounds outstandingly absorb and poorly transmit in this range. Fig. 10 also shows that all compounds exhibit strong absorption in the visible range which make them efficient for solar cell applications.

3.5 Simulation and modelling of solar cell

The optimization of the electrical parameters of the solar cells investigated in this study is carried out using the SCAPS-1D. The cell structure is shown in Fig. 11 and the input parameters of the different layers are in Table 1 and Table S1 to S3 while the input parameters of the interface defect layers in Table 2.

3.5.1 ETL and HTL optimization. The aim is to design the suitable solar cell with the best electrical parameters and PV characteristics.[46] Here, several HTLs and ETLs are incorporated in order to produce all the feasible combinations of solar cell devices. All the input data of different ETLs and HTLs respectively are collected and given in Tables S1 to S3 which are employed in SCAPS simulations for different FTO/ETL/$K_3Ti_2Cl_{9-x}Br_x$ (x = 0, 3, 6 and 9)/HTL structures.

This study examines the effects of some selected HTLs, such as CFTS CuO_2, CuI, CuSCn, MoO_3, NiO, rGO, PEDOT:PSS and P3HT, $K_3Ti_2Cl_{9-x}Br_x$ (x = 0, 3, 6 and 9) as the absorbers, some selected ETLs, such as the TiO_2, Li doped TiO_2, ZnO, Al doped

Table 6 Simulation parameters of WS_2 as ETL with different HTL for $K_3Ti_2Cl_{9-x}Br_x$ (x = 0, 3, 6, 9) perovskite as absorber layer

HTL	ETL		V_{oc} (V)	J_C (mA cm^{-2})	FF (%)	PCE (%)
CFTS	WS_2	$K_3Ti_2Cl_9$	0.34	19.37	46.58	3.12
		$K_3Ti_2Cl_6Br_3$	0.34	24.26	45.25	3.81
		$K_3Ti_2Cl_3Br_6$	0.34	26.37	44.75	4.09
		$K_3Ti_2Br_9$	0.77	17.79	75.54	12.24
Cu_2O		$K_3Ti_2Cl_9$	1.20	16.98	78.45	16.03
		$K_3Ti_2Cl_6Br_3$	1.11	22.76	77.27	19.64
		$K_3Ti_2Cl_3Br_6$	1.04	25.20	75.65	19.94
		$K_3Ti_2Br_9$	0.99	26.92	74.43	20.04
CuSCn		$K_3Ti_2Cl_9$	0.91	17.79	75.54	12.24
		$K_3Ti_2Cl_6Br_3$	0.91	22.73	73.70	15.25
		$K_3Ti_2Cl_3Br_6$	0.90	25.21	73.83	16.80
		$K_3Ti_2Br_9$	0.89	26.96	74.29	17.92
MoO_3		$K_3Ti_2Cl_9$	1.18	16.72	78.64	15.53
		$K_3Ti_2Cl_6Br_3$	1.0	22.76	78.48	19.37
		$K_3Ti_2Cl_3Br_6$	1.04	25.20	75.91	19.95
		$K_3Ti_2Br_9$	1.32	21.57	82.65	23.62
NiO		$K_3Ti_2Cl_9$	1.05	17.81	78.25	14.68
		$K_3Ti_2Cl_6Br_3$	1.03	22.85	77.71	18.34
		$K_3Ti_2Cl_3Br_6$	1.02	25.29	75.97	19.63
		$K_3Ti_2Br_9$	1.00	27.00	73.86	20.01
rGO		$K_3Ti_2Cl_9$	0.84	17.24	68.46	9.99
		$K_3Ti_2Cl_6Br_3$	0.85	22.56	67.53	13.00
		$K_3Ti_2Cl_3Br_6$	0.85	25.04	67.33	14.42
		$K_3Ti_2Br_9$	0.85	26.76	67.56	15.40
PEDOT:PSS		$K_3Ti_2Cl_9$	0.91	25.17	77.81	20.57
		$K_3Ti_2Cl_6Br_3$	0.92	23.39	74.93	6.15
		$K_3Ti_2Cl_3Br_6$	0.92	25.34	74.97	17.53
		$K_3Ti_2Br_9$	0.92	26.98	74.85	18.66
P3HT		$K_3Ti_2Cl_9$	0.64	17.85	68.12	8.92
		$K_3Ti_2Cl_6Br_3$	0.64	22.8v	67.79	10.03
		$K_3Ti_2Cl_3Br_6$	0.64	25.24	67.57	11.06
		$K_3Ti_2Br_9$	0.64	26.96	67.03	11.71

© 2026 The Author(s). Published by the Royal Society of Chemistry

Open Access Article. Published on 03 June 2026. Downloaded on 6/16/2026 1:54:48 AM. This article is licensed under a Creative Commons Attribution-NonCommercial 3.0 Unported Licence.

ZnO, C_{60}, IGZO, PCBM, SnO_2, WS_2 as ETL, PCBM-PCPB, PCBM-SnS_2 and TiO_2-SnO_2 as hybrid ETL and Cu as the back contact to examine the PV performance parameters of the $K_3Ti_2Cl_{9-x}Br_x$ (x = 0, 3, 6 and 9)-based solar cells. Here, fifty four combinations of ETL/$K_3Ti_2Cl_{9-x}Br_x$ (x = 0, 3, 6 and 9)/HTL heterojunction structures are designed. The PV characteristics of the various designed solar cells by considering all combinations of HTLs and ETLs and their PV characteristics, are given in Tables 4–6. From the tables it is well noticeable that among all the $K_3Ti_2Cl_{9-x}Br_x$ (x = 0, 3, 6 and 9)-based solar cell structures, the WS_2/$K_3Ti_2Cl_{9-x}Br_x$ (x = 0, 3, 6 and 9)/CuI configuration with CuI HTL and WS_2 ETL provides the highest performance with an efficiency of 18.52, 24.16, 25.25 and 29.34%, FF of 81.36, 81.63, 79.78 and 79.58%, V_{oc} of 1.28, 1.29, 1.25 and 1.35 V and J_{sc} of 17.77, 22.87, 25.29 and 27.00 mA cm^{-2} indicating WS_2 and CuI as the best ETL and HTL for these absorbers.

3.5.2 Effect of absorber layer thickness on the performance of the devices. Device performance, material consumption, and cost are all impacted by thickness. The ideal thickness of the absorber in solar cell devices is determined by balancing absorption and recombination; this allows for effective charge collection.[47] These devices are simulated to determine the best range of absorber layer thickness for $K_3Ti_2Cl_{9-x}Br_x$ (x = 0, 3, 6 and 9). Throughout the course of the simulation, the absorber layer's thickness was adjusted between 200 nm and 2000 nm. Parameters, including J_{sc} and η are found to rise as the absorber thickness is raised, according to the simulation findings displayed in tables S4 to S7. A high absorption coefficient causes an increase in the formation of electron–hole pairs as a result of the absorption of more photons with longer wavelengths, which happens when the thickness is raised. On the other hand the V_{oc} and FF shown an increasing nature for $K_3Ti_2Cl_9$ and decreasing nature for other absorbers is due to reduced interfacial recombination and high photon absorption and behaves in the opposite nature for other absorbers. Additionally, FF follows the same trends due to the lower and higher series resistance. A thickness of approximately 1500 nm seems to be adequate to attain a good efficiency due to the slower growth rate of device efficiency, which is enough to absorb the majority of incident photons.

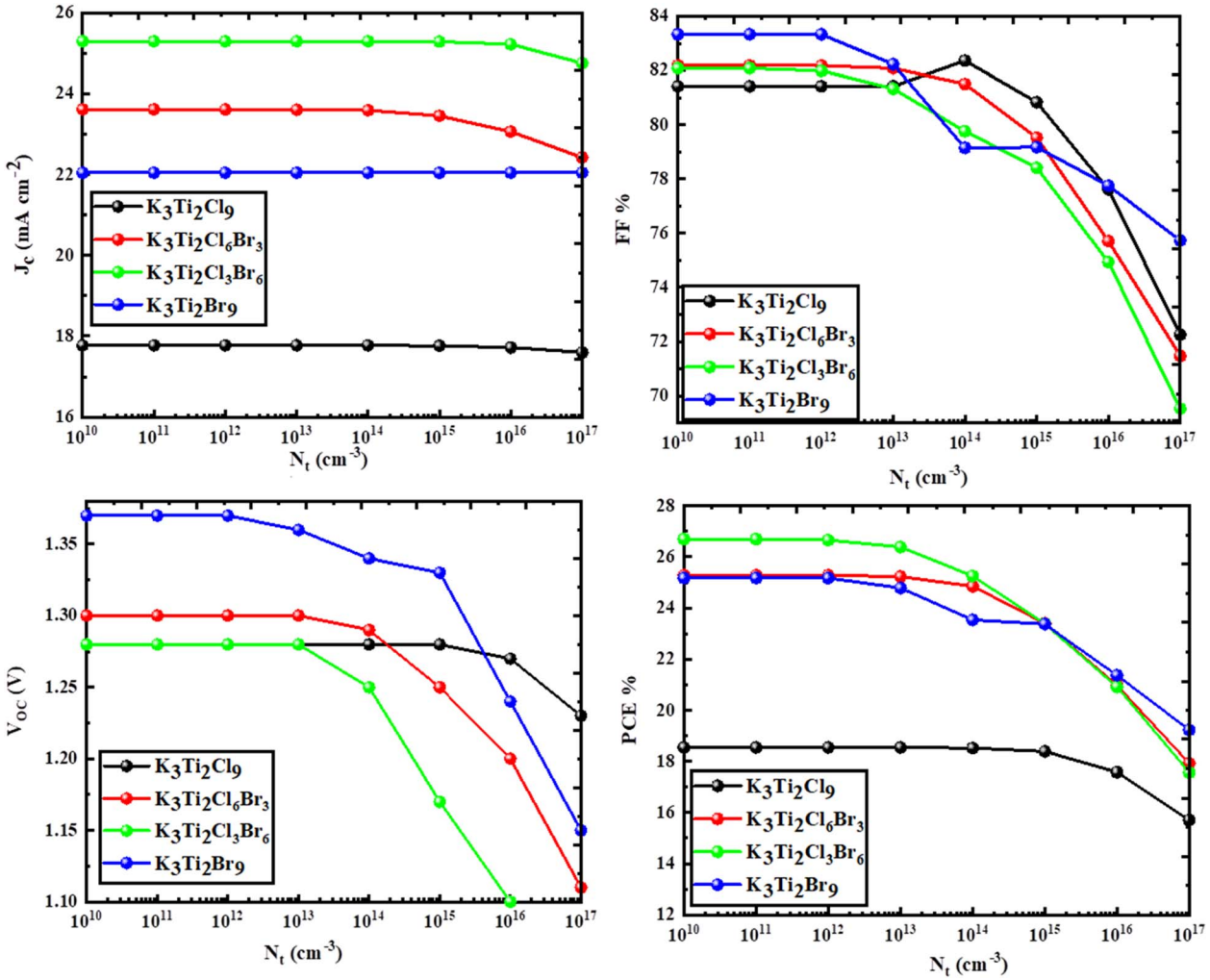

Fig. 13 Effect of accepter carrier concentration on the PV parameters of the $K_3Ti_2Cl_{9-x}Br_x$ (x = 0, 3, 6 and 9) halide perovskites.

© 2026 The Author(s). Published by the Royal Society of Chemistry

Open Access Article. Published on 03 June 2026. Downloaded on 6/16/2026 1:54:48 AM. This article is licensed under a Creative Commons Attribution-NonCommercial 3.0 Unported Licence.

3.5.3 Influence of the density of defects on the $K_3Ti_2Cl_{9-x}Br_x$ (x = 0, 3, 6 and 9) absorber layer. Defect states in the bulk material and the interface have a substantial impact on the optoelectronic characteristics of semiconductor compounds in thin films.[48] In this stage, we quantitatively analyzed the impact of defect states on the performance of solar cells. We adjusted the defect density from 10^{10} cm^{-3} to 10^{17} cm^{-3}, while keeping all other input values constant. The variations in V_{oc}, J_{sc}, FF, and η in relation to the density of neutral defects are shown in Fig. 13 and Tables S8 to S11. When the defect density is less than 10^{12} cm^{-3}, the total cell performance is constant. However, when N_t increases, the performance drops significantly. The efficiency of $K_3Ti_2Cl_{9-x}Br_x$ (x = 0, 3, 6 and 9) is merely 18.54 to 25.70% when the defect density is 10^{10} cm^{-3}. An increase in defect density results in a decrease in the diffusion length of electrons and holes and the addition of a recombination carrier to the absorber layer, both of which have a direct impact on efficiency.

3.5.4 Effect of doing acceptor carrier concentration on device performance. There are a number of variables that influence SC performance, but doping is among the most important.[48] Fig. 14 and Tables S8 to S11 displays the change in cell characteristics as a function of the absorber layer's acceptor carrier concentration (N_A), with doping levels ranging from 10^{10} to 10^{20} cm^{-3}. Up to 10^{15} cm^{-3} the J_{sc} is almost constant and then decreases due to an increase in free charge recombination. Additionally, all the other cell parameters are increasing as a function of the N_A. The overall efficiency of the SC is enhanced as the acceptor concentration increases since cell characteristics like FF and V_{oc} also increase. V_{oc} increases as the concentration of acceptor doping increases because the hole's Fermi energy level falls.

3.5.5 A device's efficiency as a function of series and shunt resistance. The device's performance is heavily affected by the series and shunt resistance. While in a perfect solar cell the series and shunt resistances would be infinite and zero respectively but in reality they would have an effect. The

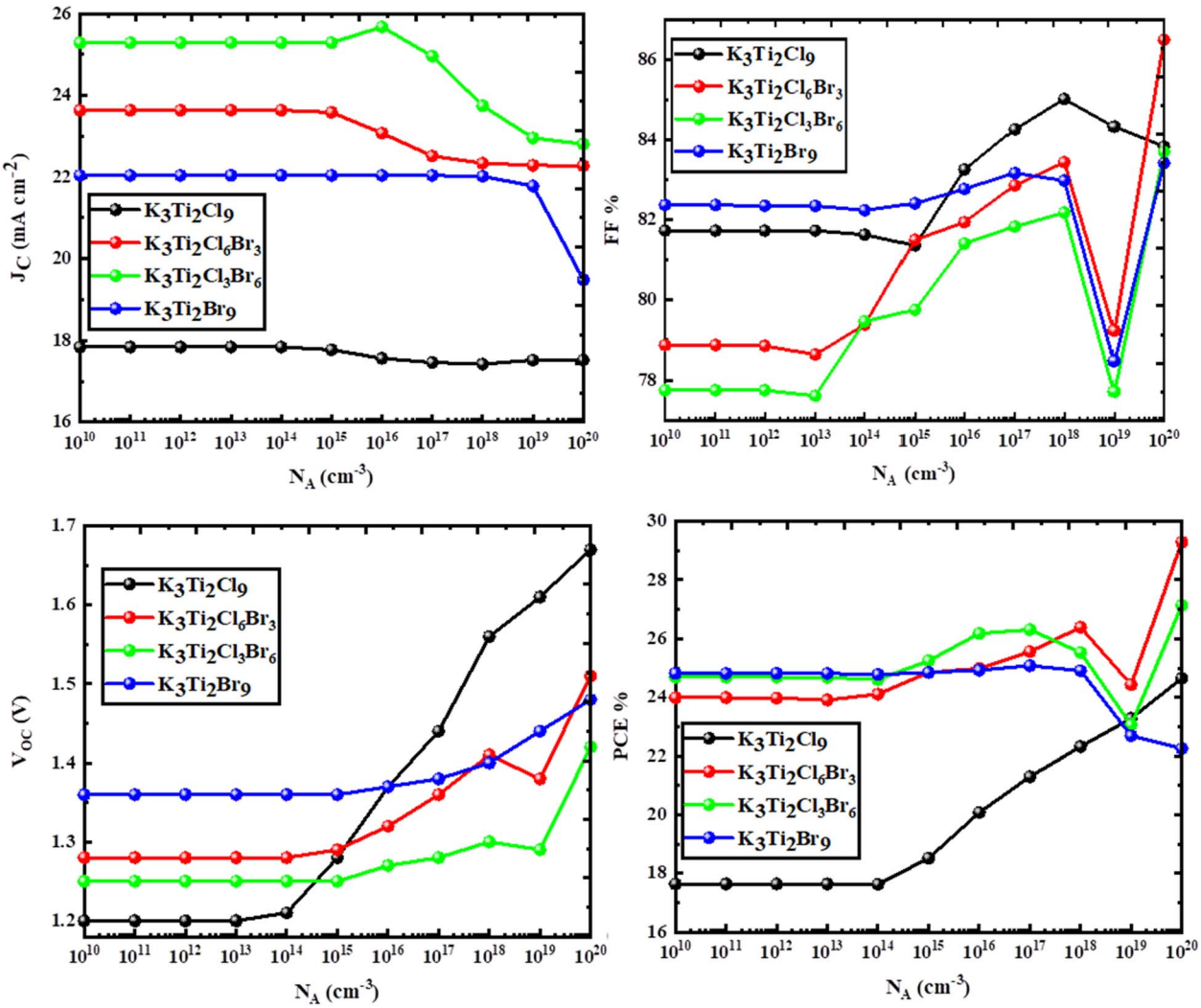

Fig. 14 Effect of defect density on the PV parameters of the $K_3Ti_2Cl_{9-x}Br_x$ (x = 0, 3, 6 and 9) halide perovskites.

Open Access Article. Published on 03 June 2026. Downloaded on 6/16/2026 1:54:48 AM.
This article is licensed under a Creative Commons Attribution-NonCommercial 3.0 Unported Licence.

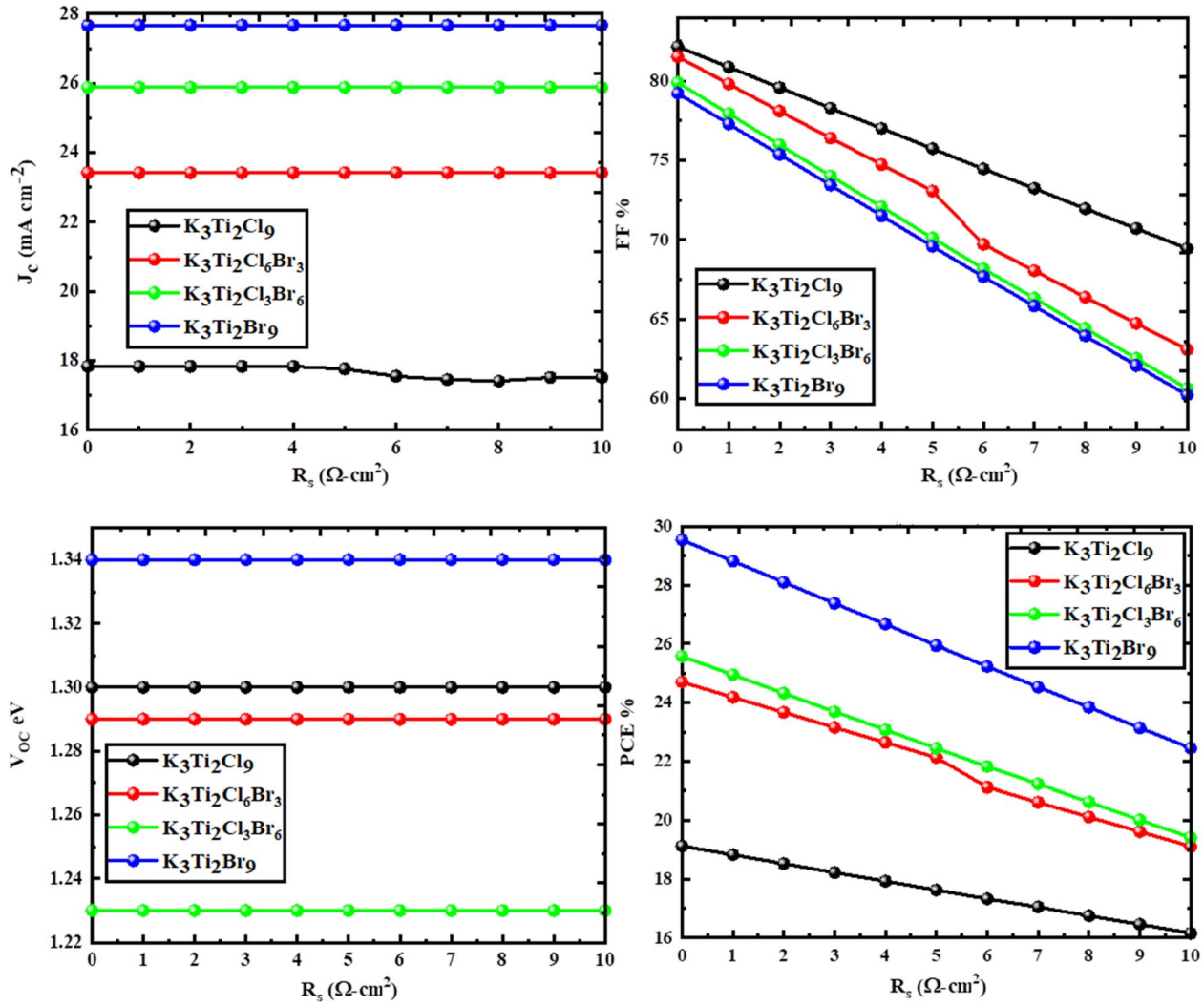

Fig. 15 Effect of series resistance on the PV parameters of the $K_3Ti_2Cl_{9-x}Br_x$ (x = 0, 3, 6 and 9) halide perovskites.

resistance in series is comprised of the bulk layers, electrodes and charge generation's interface resistance.[49] In contrast, shunt resistance is the obstacle that cells with faulty states face when trying to arise from recombination. A higher shunt resistance is indicative of a less faulty state.[49] Its performance is impacted by the SC's imperfection. The effect of series and shunt resistance on the cell's photovoltaic characteristics is seen in Fig. 15, 16 and Tables S12 to S15 respectively. From 0 to 10 Ω cm^2, the fill factor and efficiency diminish as the series resistance increases. Be that as it may, V_{oc} and J_{sc} are unchanging. At 0 Ω cm^2, the maximum value of efficiency is 19.12, 24.70, 25.58 and 29.54% and reduce 16.15, 19.11, 19.41 and 22.45% respectively while the maximum value of FF in the range of 79.24 to 82.16% and then reduces accordingly with rises in R_s. One possible explanation for the drop in FF as series resistance increases is a decline in maximum output power.

Fig. 16 show the effect of shunt resistance (R_{sh}) on the PV parameters of these compounds set from 101 to 108 Ω cm^2. All the PV parameters increase up to certain value and then become constant as the R_{sh} rises. FF rises as R_{sh} rises because SC's power output improves due to less leakage current. The data shown above indicate that the device's J_{sc} are unaffected by shunt resistance. It follows that the study showed that the PCE of the SC can be further improved by raising shunt resistance and lowering series resistance. In addition, there appears to be a saturation point beyond which the variation of efficiency and FF with shunt resistance no longer increases.

3.5.6 Effect of recombination on the device's performance. The recombination rate and its impact on the cell's performance are determined by considering the radiative and Auger recombination coefficients.[50] The recombination parameters for the absorbers are shown in Table 8. Similarly, the radiative coefficients (B_r) for these compounds are 1.76 × 10^{-9}, 1.51 × 10^{-9}, 1.27 × 10^{-9} and 1.05 × 10^{-9} photons cm^3 s^{-1} and the non-radiative Auger recombination is also taken in to account and optimized for these compounds both for holes and electrons in the range from 10^{-29} to 10^{-31} cm^6 s^{-1} to evaluate its effect on the SC parameters for these absorbers. The PV

© 2026 The Author(s). Published by the Royal Society of Chemistry

Open Access Article. Published on 03 June 2026. Downloaded on 6/16/2026 1:54:48 AM.
This article is licensed under a Creative Commons Attribution-NonCommercial 3.0 Unported Licence.

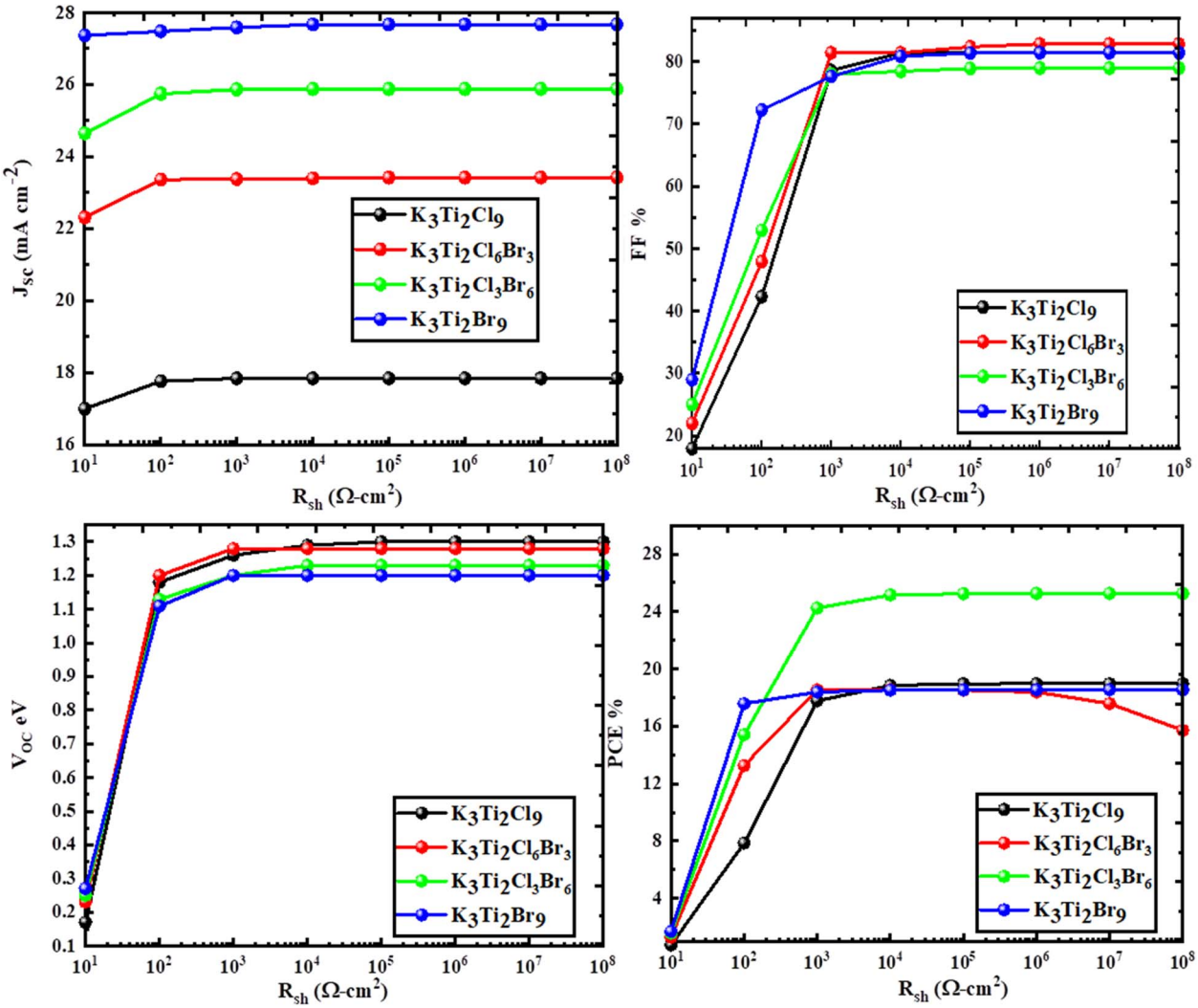

Fig. 16 Effect of shunt resistance on the PV parameters of the $K_3Ti_2Cl_{9-x}Br_x$ (x = 0, 3, 6 and 9) halide perovskites.

Table 7 Calculated solar to chemical efficiency for the $K_3Ti_2Cl_{9-x}Br_x$ (x = 0, 3, 6, 9) compounds

Parameters	ΔG $_{Product}$ (V)	$K_3Ti_2Cl_9$	$K_3Ti_2Cl_3Br_6$	$K_3Ti_2Cl_3Br_6$	$K_3Ti_2Br_9$	For other materials
η ($H_2O \rightarrow H_2$)	1.23	21.89%	28.13%	31.10%	33.21%	2.07% (ref. 57),11.5% (ref. 58), 17% (ref. 59)
η ($CO_2 \rightarrow CH_4$)	0.24	4.27%	5.48%	6.06%	6.48%	
η ($CO_2 \rightarrow CH_4OH$)	0.39	6.94%	8.91%	9.86%	10.53%	
η ($N_2 \rightarrow NH_3$)	0.10	1.78%	2.28%	2.25%	2.70%	1.48% (ref. 60), 0.24% (ref. 61)

Table 8 Radiative and Auger recombination parameters of the $K_3Ti_2Cl_{9-x}Br_x$ (x = 0, 3, 6 and 9) compound

Parameters	$K_3Ti_2Cl_9$	$K_3Ti_2Cl_6Br_3$	$K_3Ti_2Cl_3Br_6$	$K_3Ti_2Br_9$
Radiative coefficient (B_r cm^3 s^{-1})	1.76×10^{-9}	1.51×10^{-9}	1.27×10^{-9}	1.05×10^{-9}
Auger coefficient for electron (C_n cm^6 s^{-1})	10^{-29} to 10^{-31}	10^{-29} to 10^{-31}	10^{-29} to 10^{-31}	10^{-29} to 10^{-31}
Auger coefficient for hole (C_p cm^6 s^{-1})	10^{-29} to 10^{-31}	10^{-29} to 10^{-31}	10^{-29} to 10^{-31}	10^{-29} to 10^{-31}

© 2026 The Author(s). Published by the Royal Society of Chemistry

Open Access Article. Published on 03 June 2026. Downloaded on 6/16/2026 1:54:48 AM. This article is licensed under a Creative Commons Attribution-NonCommercial 3.0 Unported Licence.

Table 9 Simulation parameters for initial configuration, after thickness optimization and with recombination coefficients for $K_3Ti_2Cl_{9-x}Br_x$ (x = 0, 3, 6 and 9) perovskite as absorber layer

Parameters	$K_3Ti_2Cl_9$	$K_3Ti_2Cl_6Br_3$	$K_3Ti_2Cl_3Br_6$	$K_3Ti_2Br_9$
Initial configuration after EHL and HTL optimization				
Thickness (nm)	900	900	900	900
ETL	WS_2	WS_2	WS_2	WS_2
HTL	CuI	CuI	CuI	CuI
V_{oc} (V)	1.28	1.29	1.25	1.35
J_{sc} (mA cm^{-2})	17.77	22.87	25.29	27.00
FF (%)	81.36	81.63	79.76	79.58
PCE (%)	18.52	24.16	25.25	29.34
After thickness optimization				
Thickness (nm)	1500	1500	1500	1500
V_{oc} (V)	1.30	1.29	1.23	1.34
J_C (mA cm^{-2})	17.84	23.42	25.88	27.67
FF (%)	82.16	81.53	79.92	60.15
PCE (%)	19.12	24.70	25.58	29.54
With calculated recombination coefficients				
Thickness (nm)	1500	1500	1500	1500
V_{oc} (V)	1.30	1.29	1.23	1.31
J_C (mA cm^{-2})	17.84	23.42	25.88	27.00
FF (%)	82.14	81.53	80.09	62.07
PCE (%)	19.11	24.68	25.51	29.00

parameters after applying the recombination coefficients are given in Table 9 in addition to parameters obtained through 900 and 1500 nm thickness. From the table it is clear that recombination slightly effect the PV parameters indicating the good optimization of the solar cell design.

The J–V characteristics of $K_3Ti_2Cl_{9-x}Br_x$ (x = 0, 3, 6 and 9)-based solar cell $WS_2/K_3Ti_2Cl_{9-x}Br_x$ (x = 0, 3, 6 and 9)/CuI configuration with the addition of recombination effect is shown in Fig. 17 provides the highest performance with an efficiency of 19.11, 24.68, 25.51 and 29.00%, FF of 82.14, 81.53, 80.09 and 62.07%, V_{oc} of 1.30, 1.29, 1.23 and 1.35 V and J_{sc} of 17.84, 23.42, 25.88 and 27.00 mA cm^{-2} indicating WS_2 and CuI as the best ETL and HTL for these absorbers. On the other hand WS_2 also acts as a good ETL for the isotropic compound.[51,52]

The EQE form Fig. 18 for $K_3Ti_2Cl_{9-x}Br_x$ (x = 0, 3, 6 and 9) absorber ranges from 11.88 to 57.60% at 4.1 eV, reaches 99.38 to 99.02 and 100% between 3.44-2.38 eV and then drops to 43.21% at 1.82 eV for $K_3Ti_2Cl_9$, for $K_3Ti_2Cl_6Br_3$ to 55.51% at 1.65 eV, for $K_3Ti_2Cl_3Br_6$ to 50.60% at 1.56 eV and reduces for $K_3Ti_2Br_9$ up to 22.88% at 1.51 eV. In the visible light range, the device transforms photons into practical electricity with relative ease. Nevertheless, the QE begins to fall as the energy falls and the wavelengths grow longer. A key component in determining the photovoltaic properties, especially the PCE, is the control of electron flow to minimize energy losses produced by the HTL.

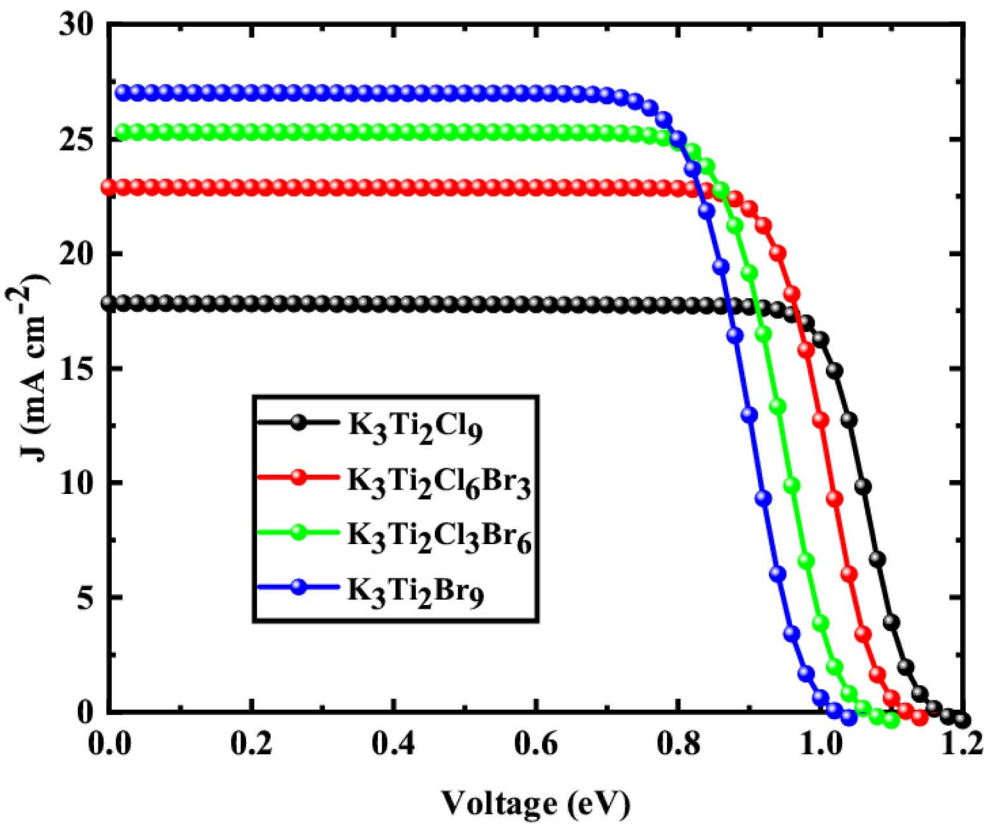

Fig. 17 J–V curve of the optimized $K_3Ti_2Cl_{9-x}Br_x$ (x = 0, 3, 6 and 9) halide perovskites.

© 2026 The Author(s). Published by the Royal Society of Chemistry

Open Access Article. Published on 03 June 2026. Downloaded on 6/16/2026 1:54:48 AM.
This article is licensed under a Creative Commons Attribution-NonCommercial 3.0 Unported Licence.

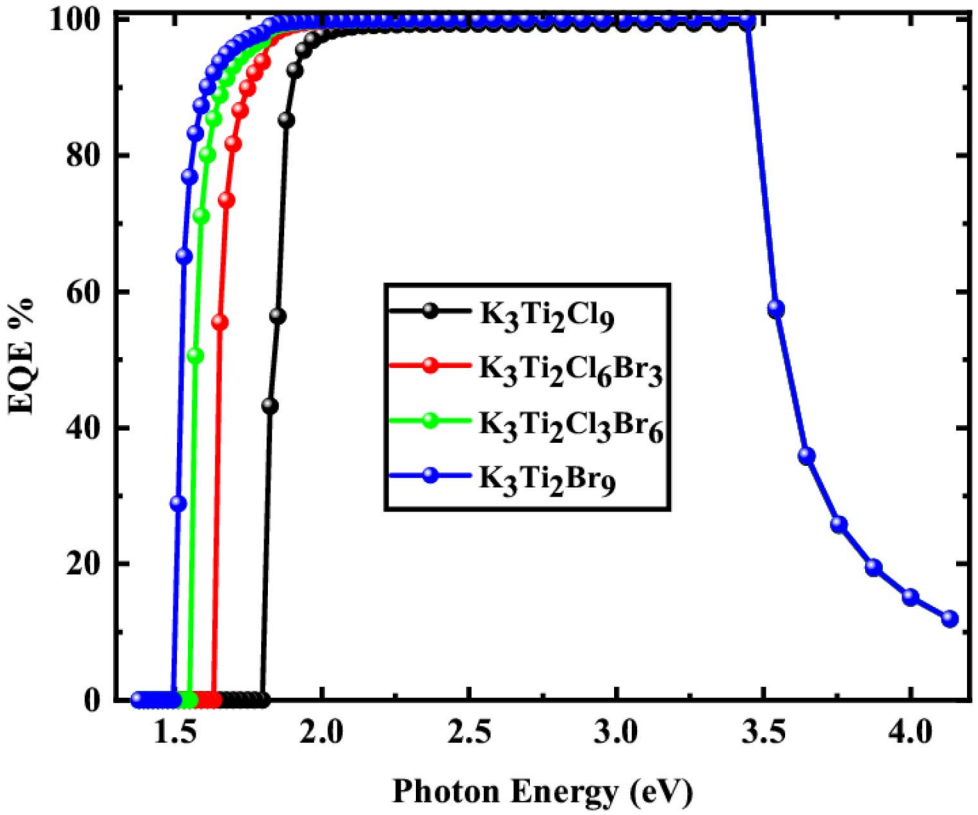

Fig. 18 EQE curve of the optimized $K_3Ti_2Cl_{9-x}Br_x$ (x = 0, 3, 6 and 9) halide perovskites.

3.5.7 Band structure. The energy band diagram for the simulated $K_3Ti_2Cl_{9-x}Br_x$ (x = 0, 3, 6 and 9) based device employing CuI as the HTL and WS_2 as the ETL is shown in Fig. 19. Based on observations, lead-free PSCs with band gaps between 1.3 to 2.15 eV produce superior photovoltaic results. Our computed device meets this requirement, with an E_g of 1.86 to 1.51 eV for the $K_3Ti_2Cl_{9-x}Br_x$ (x = 0, 3, 6 and 9) absorbers and improved PV performance. In addition, it is crucial to ensure that the band gaps of the HTL, ETL, and absorber layers are properly matched in order to avoid charge recombination and maximize carrier extraction from the interfaces of different layers within the device structure. This is accomplished by taking into account the valence band offset (VBO) between the HTL and absorber layer and the conduction band offset (CBO) between the ETL and absorber layer. As a result of the electron affinity of the ETL, HTL, and absorber layers, the barrier height at interfaces created by photo-generated carriers determines the value of CBO and VBO. A tiny positive value for VBO and a negative value for CBO can improve PSC performance, since a high VBO will impede hole conduction from the absorber to the HTL and a negative VBO will enhance carrier recombination. A spike at the perovskite/ETL interface while the perovskite/HTL shows the cliff is shown in Fig. 19 as their CBO becomes positive and VBO becomes negative.[53] In this case, E_c, E_v, E_n and E_p stand for the energy levels of the conduction band, valence band, and Fermi level in n-type and p-type materials, respectively. The band structure shows the alignment of the VB between the HTL and the absorber layer, as well as the alignment of the CB between the ETL and the absorber layer.

3.6 Photocatalytic properties

Photocatalytic reactions can only occur in materials with superior optical and electrical properties. Crystals with optimum bandgap (E_g), band edge levels (BEL), optical absorbance (GA), and effective carrier masses (ECM) may be able to split water photocatalytically. The most important thing is that each of these perovskites has an appropriate E_g between 1.5 and 3.0 eV.

The Mulliken electronegativity technique is used to study the photocatalytic properties of these 2D perovskites in order to determine their water-splitting potential. Estimates of the ECB and EVB are derived respectively. The geometric mean of an electronegativity, represented by χ, is 5.31, 5.26, 5.21 and 5.16 eV for $K_3Ti_2Cl_{9-x}Br_x$ (x = 0, 3, 6 and 9) is a crucial component in figuring out an electron's electrical characteristics and free energy.[54] For these semiconductor materials to effectively split water photocatalytically, their VBM and CBM must be larger than or equal to the redox potential of H^*/H_2 (0 V against NHE).[55] CO_2 and N_2 can also be reduced photocatalytically using these methods. These materials have oxygen potentials (EVB) greater than 1.23 V and hydrogen redox potentials (ECB) lower than 0 V and are feasible for

Open Access Article. Published on 03 June 2026. Downloaded on 6/16/2026 1:54:48 AM.
This article is licensed under a Creative Commons Attribution-NonCommercial 3.0 Unported Licence.

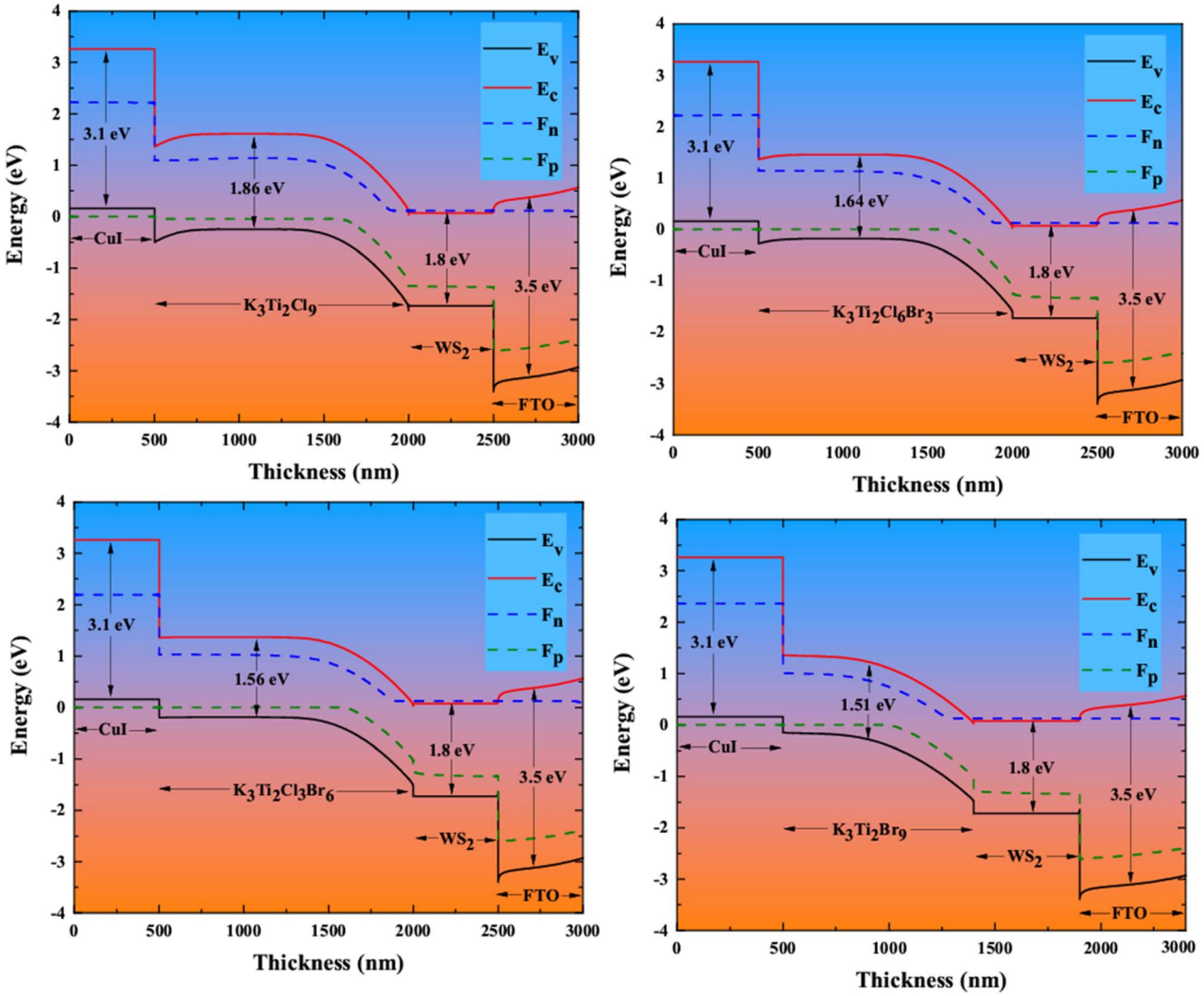

Fig. 19 Band structure of the $K_3Ti_2Cl_{9-x}Br_x$ (x = 0, 3, 6 and 9) halide perovskites.

photocatalytic water splitting, as shown in Fig. 20, when exposed to visible light. In addition, as shown in Fig. 20, the EVB of all perovskites is more negatively correlated with CO_2 reduction, which can photo-reduce CO_2 more easily than CO_2/CH_4OH, and CO_2/CH_4. Similarly, when evaluating N_2, it can photo-reduce to NH_3. Therefore, the compounds are feasible under ideal conditions at PH = 0, in assessing oxygen, splitting water, decreasing CO_2 and fixing nitrogen, in that order. The reduction products, however, should be used with consideration and treated accordingly to ensure that they do not harm the environment.

Furthermore Table 7 displays the computed solar to chemical efficiency (STC) and the value of J_{sc} is displayed in Fig. 12, both of which are used to assess the photocatalytic performance of these compounds. The compounds in consideration have η ($H_2O \rightarrow H_2$) values of 21.89, 28.13, 31.10 and 33.21% respectively, which exceed the 10% threshold value for commercial usage[56] and two-dimensional compounds.[57–59]

In the same way, the η values for $CO_2 \rightarrow CH_4$ is 4.27, 5.48, 6.06 and 6.48%, for $CO_2 \rightarrow CH_4OH$ is 6.94, 8.91, 9.86 and 1.53% and η for $N_2 \rightarrow NH_3$ are 1.78, 2.28, 2.25 and 2.70% respectively. The reported values for these compounds are significantly higher than the other 2D materials' reported values of 0.24% and 1.48%.[60,61]

Anion substitution consistently improves photocatalytic activity when compared to pure $K_3Ti_2Cl_9$, according to the computed solar-to-chemical efficiencies. The η values for water splitting, carbon dioxide reduction, and nitrogen fixation are greater in $K_3Ti_2Cl_{9-x}Br_x$ (x = 0, 3, 6 and 9) compared to other 2D materials that have been reported. Additionally, for hydrogen evolution, they surpass the 10% industrial benchmark. Cation disorder-induced changes to the electronic structure are responsible for this enhancement; they lead to better charge separation and stronger light absorption, which in turn boost reaction efficiencies in various reduction pathways.

© 2026 The Author(s). Published by the Royal Society of Chemistry

Open Access Article. Published on 03 June 2026. Downloaded on 6/16/2026 1:54:48 AM.
This article is licensed under a Creative Commons Attribution-NonCommercial 3.0 Unported Licence.

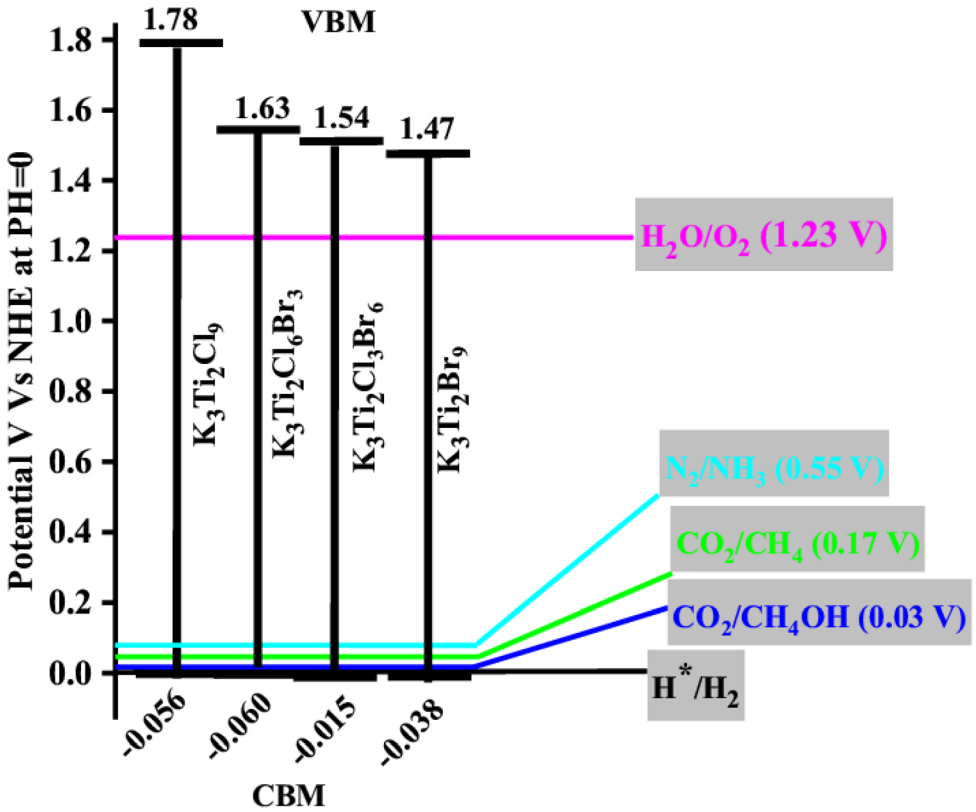

Fig. 20 Band edges of the $K_3Ti_2Cl_{9-x}Br_x$ (x = 0, 3, 6 and 9) halide perovskites compared to the redox potentials of the water-splitting reaction, CO_2 reduction and N_2 fixation photo degradation processes at normal hydrogen electrode (NHE) scale at pH = 0.

4 Conclusions

These halide $K_3Ti_2Cl_{9-x}Br_x$ (x = 0, 3, 6 and 9) perovskites are studied structurally and optoelectronically using the FPLAPW method in the DFT domain with GGA and TB-mBJ potentials. The structural parameters computed by WIEN2k match the experimental data to a tee. According to band structure TDOS and PDOS computations, all of these compounds have a direct band gap of 1.861, 1.648, 1.577, 1.519 eV along *M*–*M* symmetry and an indirect band gap of 1.861, 1.643, 1.567 and 1.512 eV at the *M*–*K* symmetry. Optoelectronic devices and SC applications are ideal for these compounds because of their visible-light optical dynamics. The SCAPS-1D program is employed to identify the optimal solar cell designs that integrate various ETLs and HTLs. The structure with the highest power conversion efficiency out of the fifty four configurations examined is FTO/WS_2/$K_3Ti_2Cl_{9-x}Br_x$ (x = 0, 3, 6 and 9)/CuI, providing the highest performance with an efficiency of 19.11, 24.68, 25.25 and 29.00%, FF of 82.14, 81.53, 80.09 and 62.07%, V_{oc} of 1.30, 1.29, 1.25 and 1.35 V and J_{sc} of 17.84, 23.42, 25.88 and 27.00 mA cm^{-2} with the addition of the recombination effect. On the other hand, the effect of thickness, defect density, series and shunt resistance is also examined. Photocatalytic analysis shows that all of these compounds are capable of converting H_2O to O_2 and H_2. In the same way that the compounds under study may reduce N_2 to NH_3, they can likewise reduce CO_2 to CH_4OH and CH_4. In comparison to other materials, these compounds have an effective efficiency for reducing CO_2 and N_2 and their photocatalytic efficiency for water splitting is higher than the intended value for industrial application. The findings of this study paves the way for lead-halide-free, entirely inorganic perovskite photovoltaics and photocatalysts. Such materials would exhibit enhanced photovoltaic and photocatalytic performance and could be used in various fields such as optoelectronics, photovoltaics, and photocatalysis, especially those involving visible light-driven processes like water splitting, CO_2 reduction, and N_2 fixation.

Author contributions

Shahid Mehmood handle the formal analysis, research techniques and writing (first draft). Shah Rukh Khan performs the investigation, research data collection, methodology and writing (first draft). Shaimaa A. M. Abdelmohsen involved in leading the initial idea and design of the research manages projects, providing guidance and oversight to the research team. Meznah M. Alanazi supervise the work, provide resources and software and validate the work. Hanan Al Ghamdi handles data visualization, validation, editing and review. Mohamed Mousa is managing, cleaning and organizing research data.

Conflicts of interest

The authors stated that they have no competing interest.

Open Access Article. Published on 03 June 2026. Downloaded on 6/16/2026 1:54:48 AM. This article is licensed under a Creative Commons Attribution-NonCommercial 3.0 Unported Licence.

Data availability

The data supporting this article have been included as part of the supplementary information (SI). Supplementary information: numerical data for the optimization of different parameters of $K_3Ti_2Cl_{9-x}Br_x$-based solar cells. See DOI: https://doi.org/10.1039/d6ra01597b.

Acknowledgements

The research was funded by the Deanship of Scientific Research and Libraries at Princess Nourah bint Abdulrahman University through the Research Funding Program, Grant No. (FRP-2025-47).

References

1 Q. Jiang, Y. Zhao, X. Zhang, X. Yang, Y. Chen, Z. Chu, Q. Ye, X. Li, Z. Yin and J. You, Surface passivation of perovskite film for efficient solar cells, *Nat. Photonics*, 2019, **13**, 460–466.

2 R. Wang, J. Xue, K.-L. Wang, Z.-K. Wang, Y. Luo, D. Fenning, G. Xu, S. Nuryyeva, T. Huang and Y. Zhao, Constructive molecular configurations for surface-defect passivation of perovskite photovoltaics, *Science*, 2019, **366**, 1509–1513.

3 W. Ke and M. G. Kanatzidis, Prospects for low-toxicity lead-free perovskite solar cells, *Nat. Commun.*, 2019, **10**, 965.

4 R. Wang, J. Wang, S. Tan, Y. Duan, Z.-K. Wang and Y. Yang, Opportunities and challenges of lead-free perovskite optoelectronic devices, *Trends Chem.*, 2019, **1**, 368–379.

5 C. Wu, Q. Zhang, Y. Liu, W. Luo, X. Guo, Z. Huang, H. Ting, W. Sun, X. Zhong and S. Wei, The Dawn of Lead-Free Perovskite Solar Cell: Highly Stable Double Perovskite $Cs_2AgBiBr_6$ Film, *Adv. Sci.*, 2018, **5**, 1700759.

6 P. V. Kamat, J. Bisquert and J. Buriak, Lead-free perovskite solar cells, *ACS Energy Lett.*, 2017, **2**, 904–905.

7 S. Shao, J. Liu, G. Portale, H. H. Fang, G. R. Blake, G. H. ten Brink, L. J. A. Koster and M. A. Loi, Highly reproducible Sn-based hybrid perovskite solar cells with 9% efficiency, *Adv. Energy Mater.*, 2018, **8**, 1702019.

8 N. Ito, M. A. Kamarudin, D. Hirotani, Y. Zhang, Q. Shen, Y. Ogomi, S. Iikubo, T. Minemoto, K. Yoshino and S. Hayase, Mixed Sn-Ge perovskite for enhanced perovskite solar cell performance in air, *J. Phys. Chem. Lett.*, 2018, **9**, 1682–1688.

9 C. N. Savory, A. Walsh and D. O. Scanlon, Can Pb-free halide double perovskites support high-efficiency solar cells?, *ACS Energy Lett.*, 2016, **1**, 949–955.

10 W. Gao, C. Ran, J. Xi, B. Jiao, W. Zhang, M. Wu, X. Hou and Z. Wu, High-Quality $Cs_2AgBiBr_6$ Double Perovskite Film for Lead-Free Inverted Planar Heterojunction Solar Cells with 2.2% Efficiency, *ChemPhysChem*, 2018, **19**, 1696–1700.

11 J.-C. Hebig, I. Kühn, J. Flohre and T. Kirchartz, Optoelectronic Properties of $(CH_3NH_3)_3Sb_2I_9$ Thin Films for Photovoltaic Applications, *ACS Energy Lett.*, 2016, **1**, 309–314.

12 A. K. Baranwal, H. Masutani, H. Sugita, H. Kanda, S. Kanaya, N. Shibayama, Y. Sanehira, M. Ikegami, Y. Numata and K. Yamada, Lead-free perovskite solar cells using Sb and Bi-based $A_3B_2X_9$ and A_3BX_6 crystals with normal and inverse cell structures, *Nano Convergence*, 2017, **4**, 26.

13 K. M. Boopathi, P. Karuppuswamy, A. Singh, C. Hanmandlu, L. Lin, S. A. Abbas, C. C. Chang, P. C. Wang, G. Li and C. W. Chu, Solution-processable antimony-based lightabsorbing materials beyond lead halide perovskites, *J. Mater. Chem. A*, 2017, **5**, 20843–20850.

14 F. Jiang, D. Yang, Y. Jiang, T. Liu, X. Zhao, Y. Ming, B. Luo, F. Qin, J. Fan, H. Han, L. Zhang and Y. Zhou, Chlorine-Incorporation-Induced Formation of the Layered Phase for Antimony-Based Lead-Free Perovskite Solar Cells, *J. Am. Chem. Soc.*, 2018, **140**, 1019–1027.

15 B. Saparov, F. Hong, J.-P. Sun, H.-S. Duan, W. Meng, S. Cameron, I. G. Hill, Y. Yan and D. B. Mitzi, Thin-Film Preparation and Characterization of $Cs_3Sb_2I_9$: A Lead-Free Layered Perovskite Semiconductor, *Chem. Mater.*, 2015, **27**, 5622–5632.

16 P. Harikesh, H. K. Mulmudi, B. Ghosh, T. W. Goh, Y. T. Teng, K. Thirumal, M. Lockrey, K. Weber, T. M. Koh and S. Li, Rb as an alternative cation for templating inorganic lead-free perovskites for solution processed photovoltaics, *Chem. Mater.*, 2016, **28**, 7496–7504.

17 B.-B. Yu, M. Liao, J. Yang, W. Chen, Y. Zhu, X. Zhang, T. Duan, W. Yao, S.-H. Wei and Z. He, Alloy-Induced Phase Transition and Enhanced Photovoltaic Performance: The Case of $Cs_3Bi_2I_{9-x}Br_x$ Perovskite Solar Cells, *J. Mater. Chem. A*, 2019, **7**, 8818–8825.

18 D. Liu, B.-B. Yu, M. Liao, Z. Jin, L. Zhou, X. Zhang, F. Wang, H. He, T. Gatti and Z. He, Self-Powered and Broadband Lead-Free Inorganic Perovskite Photodetector with High Stability, *ACS Appl. Mater. Interfaces*, 2020, **12**, 30530–30537.

19 E. E. Morgan, L. Mao, S. M. L. Teicher, G. Wu and R. Seshadri, Tunable Perovskite-Derived Bismuth Halides: $Cs_3Bi_2(Cl_{1-X}I_x)_9$, *Inorg. Chem.*, 2020, **59**, 3387–3393.

20 M. Schroeder, S. Hartwig, K. W. Kramer, S. Decurtins and H. Hillebrecht, Synthesis, Structure, and Properties of the New Mixed-Valent Dodecahalogenotrimetallate $In_4Ti_3Br_{12}$ and its Relation to Compounds $A_3Ti_2X_9$ (A = K, In; X = Cl, Br), *Inorg. Chem.*, 2012, **51**(15), 8385–8393, DOI: 10.1021/ic3009442.

21 P. Blaha, K. Schwarz, F. Tran, R. Laskowski, G. Madsen and L. D. Mark, *J. Chem. Phys.*, 2020, **152**, 07410130, DOI: 10.1063/1.5143061@jcp.2020.ESS202.

22 J. P Perdew and A. Zunger, *Phys. Rev. B:Condens. Matter Mater. Phys.*, 1981, **23**, 5048–5079, DOI: 10.1103/PhysRevB.23.5048.

23 J. P. Perdew, K. Burke and Y. Wang, *Phys. Rev. Lett.*, 1996, **54**, 16533, DOI: 10.1103/PhysRevB.54.16533.

24 A. Togo, F. Oba and I. Tanaka, First-principles calculations of the ferroelastic transition between rutiletype and CaCl2-type SiO2 at high pressures, *Phys. Rev. B:Condens. Matter Mater. Phys.*, 2008, **78**, 134106.

25 F. Tran and P. Blaha, *Phys. Rev. Lett.*, 2009, **102**, 226401, DOI: 10.1103/PhysRevLett.102.226401.

26 S. Mehmood, Z. Ali, S. R Khan, M. M Alanazi, S. A. M Abdelmohsen and M. Mousa, Unveiling 2D $Rb_3Bi_2I_6Cl_3$

 © 2026 The Author(s). Published by the Royal Society of Chemistry

Open Access Article. Published on 03 June 2026. Downloaded on 6/16/2026 1:54:48 AM. This article is licensed under a Creative Commons Attribution-NonCommercial 3.0 Unported Licence.

and $Rb_3Bi_2I_3Cl_6$ perovskites for optoelectronic, solar cell and photocatalytic applications, *RSC Adv.*, 2025, **15**, 17420, DOI: 10.1039/d5ra02328a.

27 H. Liu, T. B. Korukonda and S. Bansal, Prospects of Halide Perovskites for Solar-to-Hydrogen Production, *Nanomaterials*, 2024, **14**, 1914, DOI: 10.3390/nano14231914.

28 M. Burgelman, P. Nollet and S. Degrave, Modelling polycrystalline semiconductor solar cells, *Thin Solid Films*, 2000, **361–362**, 527–532.

29 J. P. A. Jebakumar, D. J. Moni, D. Gracia and M. D. Shallet, Design and simulation of inorganic perovskite solar cell, *Appl. Nanosci.*, 2022, **12**, 1507–1518, DOI: 10.1007/s13204-021-02268-7.

30 M. Khalid Hossain, G. F. Ishraque Toki, A. Kuddus, M. H. K. Rubel, M. M. Hossain, H. Bencherif, M. F. Rahman, M. R. Islam and M. Mushtaq, An extensive study on multiple ETL and HTL layers to design and simulation of high-performance lead-free $CsSnCl_3$-based perovskite solar cells, *Sci. Rep.*, 2023, **13**, 2521, DOI: 10.1038/s41598-023-28506-2.

31 F. Birch, Finite Elastic Strain of Cubic Crystals, *Phys. Rev.*, 1947, **71**, 809–824, DOI: 10.1103/PhysRev.71.809.

32 A. Rahman, M. Haneef and B. Amin, Cs_2KAlY_6 (Y = Cl, Br, I): A lead-free double perovskites for optoelectronic and photocatalytic applications, *Chem. Phys.*, 2026, **602**, 112975, DOI: 10.1016/j.chemphys.2025.112975.

33 S. Mehmood, Z. Ali, Y. T. Alharbi, S. Alderhami and L. Almanqur, Structural and Magneto-Elastic Properties of the Quadruple Perovskites $CaCu_3B_2Os_2O_{12}$ (B = Mn-Ni): The Heisenberg Model and DFT Study, *J. Electron. Mater.*, 2023, **52**(23), 5872–5883.

34 A. Togo, First-principles phonon calculations with phonopy and phono3py, *J. Phys. Soc. Jpn.*, 2023, **92**(1), 012001, DOI: 10.7566/JPSJ.92.012001.

35 S. A. Khandy, I. Islam, A. Laref, M. Gogolin, A. K. Hafiz and M. A. Siddiqui, Electronic structure, thermomechanical and phonon properties of inverse perovskite oxide (Na_3OCl): an ab initio study, *Int. J. Energy Res.*, 2020, **44**, 2594, DOI: 10.1002/er.4982.

36 L. Yu and A. Zunger, Identification of potential photovoltaic absorbers based on first-principles spectroscopic screening of materials, *Phys. Rev. Lett.*, 2012, **108**, 068701, DOI: 10.1103/PhysRevLett.108.068701.

37 R. Sa, K. Cao, H. Zhang, L. Wu, X. Dai and D. Liu, Investigation of structural transition and indirect-direct bandgap tuning of $Cs_2Au^IAu^{III}X_6$ (X = Cl, Br, I) via single-atom doping, *Mater. Sci. Semicond. Process.*, 2025, **192**, 109447, DOI: 10.1016/j.mssp.2025.109447.

38 Bhawna, A. Alam and M. Aslam, Halide Double Perovskites: Insights into Structure, Defects, and Luminescence, *ACS Appl. Mater. Interfaces*, 2026, **18**(7), 10681–10724, DOI: 10.1021/acsami.5c20712.

39 A. Jain, O. Voznyy and E. H. Sargent, High-Throughput Screening of Lead-Free Perovskite-Like Materials for Optoelectronic Applications, *J. Phys. Chem. C*, 2017, **121**(13), 7183–7187, DOI: 10.1021/acs.jpcc.7b02221.

40 R. A. Gouvêa, *Exploring Cs3Sb2X9-type Perovskites (X = Cl, Br, I) for Optoelectronic Applications : a Theoretical Investigation Using Density Functional Theory (DFT) and Machine Learning 2024*, https://hdl.handle.net/10183/276805.

41 S. Mehmood, Z. Ali, S. R Khan, M. M Alanazi, S. A. M Abdelmohsen and M. Mousa, Improving optoelectronic and solar cell performance from 24 to 31 % via switching from 0D $Cs_3Bi_2I_9$ to 2D $Cs_3Bi_2I_6Cl_3$ perovskite for energy harvesting application, *Comput. Condens. Matter*, 2025, **44**, e01059, DOI: 10.1016/j.cocom.2025.e01059.

42 R. D. Grimes and E. R. Cowley, A Model Dielectric Function for Semiconductors, *Can. J. Phys.*, 1975, **53**, 2549–2554, DOI: 10.1139/p75-311.

43 A. Crovetto and O. Hansen, *Sol. Energy Mater. Sol. Cells*, 2017, **169**, 177–194.

44 V. S. Zakhvalinskii, T. T. Hnguyen, T. T. Pham, N. T. Dang, E. A. Piliuk and S. V. Taran, *J. Electron. Mater.*, 2017, **46**, 3523–3530, DOI: 10.1007/s11664-017-5297-z.

45 J. P. Leitão, N. M. Santos, P. A. Fernandes, P. M. P. Salomé, A. F. da Cunha, C. González, G. M. Ribeiro and F. M. Matinaga, *Phys. Rev. B:Condens. Matter Mater. Phys.*, 2011, **84**(2), 024120.

46 X. G. Zhao, D. Yang, Y. Sun, T. Li, L. Zhang, L. Yu and A. Zunger, *J. Am. Chem. Soc.*, 2017, **139**, 6718–6725.

47 O. Saidani Abderrahim, Y. Zitouni, G. S. Sahoo, R. Zouache, M. R. Mohammad, A. A. Alothman, S. Mohammad, M. Vimalan, G. F. I. Toki and M. K. Hossain, Numerical study of high-performance lead-free $CsSnCl_3$-based perovskite solar cells, *J. Opt.*, 2025, **54**, 904–922, DOI: 10.1007/s12596-024-01817-x.

48 D. Gogoi, M. Khalid Hossain, T. D. Das, G. F. I. Toki, M. D. Albaqami, S. Mohammad and M. R. Mohammad, Performance analysis of highly efficient lead-free perovskite solar cells: a numerical insight, *J. Opt.*, 2025, **54**, 2731–2742, DOI: 10.1007/s12596-024-01880-4.

49 G. F. I. Toki, M. K. Hossain, M. Shihab Uddin, A. M. Tawfeek, S. Rabhi, M. A. Darwish, R. Haldhar, D. K. Dwivedi, J. Madan and R. Pandey, Unveiling the potential of lead-free $Cs_2AgBi_{0.75}Sb_{0.25}Br_6$ double perovskite solar cells with multilayer charge transport for 30% efficiency, *Inorg. Chem. Commun.*, 2024, **165**, 112439, DOI: 10.1016/j.inoche.2024.112439.

50 M. S. Uddin, M. K. Hossain, M. B. Uddin, G. F. I. Toki, M. Ouladsmane, M. H. K. Rubel, D. I. Tishkevich, P. Sasikumar, R. Haldhar and R. Pandey, An In-Depth Investigation of the Combined Optoelectronic and Photovoltaic Properties of Lead-Free $Cs_2AgBiBr_6$ Double Perovskite Solar Cells Using DFT and SCAPS-1D Frameworks, *Adv. Electron. Mater.*, 2024, **10**, 2300751, DOI: 10.1002/aelm.202300751.

51 G. F. Ishraque Toki, M. Khalid Hossain, R. Pandey, S. Bhattarai, A. M. Tawfeek, S. Mohammad, A. M. J. Habib, N. Mahmud, M. F. Rahman, P. Sasikumar and H. Bencherif, Optimizing lead-free $Cs_3Bi_2I_9$ perovskite solar cells: exploring absorber and charge transport layers parameters for improved efficiency, *J. Opt.*, 2024, **53**, 4554–4570, DOI: 10.1007/s12596-023-01648-2.

Open Access Article. Published on 03 June 2026. Downloaded on 6/16/2026 1:54:48 AM.
This article is licensed under a Creative Commons Attribution-NonCommercial 3.0 Unported Licence.

52 A. Das, S. Datta Peu, M. A. M. Akanda, M. M. Salah, M. S. Hossain and B. K. Das, *Energies*, 2023, **16**(5), 2328, DOI: 10.3390/en16052328.

53 M. K. Hossain, S. Islam, M. N. Sakib, M. S. Uddin, G. F. I. Toki, M. H. K. Rubel, J. Nasrin, S. H. Shahatha, M. R. Mohammad, A. A. Alothman, C. J. Raorane, R. Haldhar and H. Bencherif, Exploring the Optoelectronic and Photovoltaic Characteristics of Lead-Free Cs_2TiBr_6 Double Perovskite Solar Cells: A DFT and SCAPS-1D Investigations, *Adv. Energy Mater.*, 2025, **11**, 2400348, DOI: 10.1002/aelm.202400348.

54 R. Yu, Q. Ruan, F. Xiao and X. Ming, First-principles study on the optoelectronic properties of the quasi-one-dimensional flexible semiconductor K_2PdPS_4I, *Results Phys.*, 2023, **47**, 106396, DOI: 10.1016/j.rinp.2023.106396.

55 M. Hariharan and R. D. Eithiraj, Comprehensive study on structural, electronic, optical, elastic, and transport properties of natural mercury sulphohalides via DFT computation, *Sci. Rep.*, 2024, **14**, 18593, DOI: 10.1038/s41598-024-69430-3.

56 C. F. Fu, J. Sun, Q. Luo, X. Li, W. Hu and J. Yang, Intrinsic Electric Fields in Two dimensional Materials Boost the Solar-to-Hydrogen Efficiency for Photocatalytic Water Splitting, *Nano Lett.*, 2018, **18**(10), 6312–6317, DOI: 10.1021/acs.nanolett.8b02561.

57 H. Fu, Q. Zhang, Y. Liu, Z. Zheng, H. Cheng, B. Huang and P. Wang, Photocatalytic Overall Water Splitting with a Solar-to-Hydrogen Conversion Efficiency Exceeding 2 % through Halide Perovskite, *Angew. Chem., Int. Ed.*, 2024, **136**, e202411016, DOI: 10.1002/anie.202411016.

58 J. Park, J. Lee, H. Lee, H. Im, S. Moon, C. S. Jeong, W. Yang and J. Moon, Hybrid Perovskite-Based Wireless Integrated Device Exceeding a Solar to Hydrogen Conversion Efficiency of 11%, *Small*, 2023, **19**, 2300174, DOI: 10.1002/smll.202300174.

59 M. Jakhar and A. Kumar, Tunable photocatalytic water splitting and solar-to-hydrogen efficiency in β-PdSe2 monolayer, *Catal. Sci. Technol.*, 2021, **11**, 6445–6454, DOI: 10.1039/D1CY00953B.

60 T. H. Liu, Y. H. Huang, Y. X. Huang, Y. S. Lu, T. M. Tsai, C. Chang, P. C. Kuo, J. Shiue, Y. C. Huang, C. W. Chen, C. C. Chen and S. S. Li, Bias-Free Solar to Ammonia Photoelectrochemical Conversion Using Perovskite-Silicon Tandem Absorber and 1T-MoS2 Integration, *J. Mater. Chem. A*, 2025, **13**, 12104–12112, DOI: 10.1039/D4TA08427F.

61 J. Zheng, L. Lu, K. Lebedev, S. Wu, P. Zhao, I. J. McPherson, T. S. Wu, R. Kato, Y. Li, P. L. Ho, G. Li, L. Bai, J. Sun, D. Prabhakaran, R. A. Taylor, Y. L. Soo, K. Suenaga and S. C. E. Tsang, Fe on molecular-layer MoS_2 as inorganic Fe-S_2-Mo motifs for light-driven nitrogen fixation to ammonia at elevated temperatures, *Chem Catal.*, 2021, **1**, 162–182, DOI: 10.1016/j.checat.2021.03.002.

© 2026 The Author(s). Published by the Royal Society of Chemistry